

The  $NOE$  detector for a long baseline  
neutrino oscillation experiment

The  $NOE$  Collaboration

(Bari - Bologna - LNGS - Lecce - IHEP - INR - ITEP - JINR -  
LPI - MEPI - Milano - Napoli - Roma)

INFN - Laboratori Nazionali del Gran Sasso





## The $NOE$ detector for a long baseline neutrino oscillation experiment

M.Ambrosio<sup>11</sup>, C.Aramo<sup>11</sup>, G.C.Barbarino<sup>11\*</sup>, P.Bernardini<sup>4</sup>, S.Bussino<sup>12</sup>, D.Campana<sup>11</sup>,  
L.De Benedictis<sup>1</sup>, G.De Cataldo<sup>1</sup>, M.De Vincenzi<sup>12,13</sup>, A.Di Credico<sup>3</sup>, C.Favuzzi<sup>1</sup>,  
P.Fusco<sup>1</sup>, N.Giglietto<sup>1</sup>, A.Grillo<sup>3</sup>, F.Guarino<sup>11</sup>, C.Gustavino<sup>3</sup>, E.Lamanna<sup>12</sup>, A.Lauro<sup>11</sup>,  
G.Mancarella<sup>4</sup>, A.Margiotta<sup>2</sup>, D.Martello<sup>4</sup>, M.N.Mazziotta<sup>1</sup>, S.Mikheyev<sup>3,6</sup>, G.Osteria<sup>11</sup>,  
A.Rainò<sup>1</sup>, U.Rubizzo<sup>11</sup>, E.Scapparone<sup>3</sup>, P.Spinelli<sup>1</sup>, M.Spurio<sup>2</sup>, A.Surdo<sup>4</sup>,  
K.V.Aleksandrov<sup>9</sup>, A.M.Baranov<sup>10</sup>, V.A.Chechin<sup>9</sup>, A.P.Chubenko<sup>9</sup>,  
A.D.Erlykin<sup>9</sup>, G.V.Gavalian<sup>13</sup>, S.V.Golovkine<sup>5</sup>, A.M.Gorine<sup>5</sup>, E.T.Gushchin<sup>10</sup>,  
V.A.Kantserov<sup>10</sup>, R.L.Kavalov<sup>13</sup>, F.F.Kayumov<sup>9</sup>, S.K.Kotel'nikov<sup>9</sup>, E.N.Kozarenko<sup>8</sup>,  
I.E.Kreslo<sup>8</sup>, E.P.Kuznetsov<sup>9</sup>, B.N.Lomonosov<sup>9</sup>, M.P.Lorikian<sup>13</sup>, A.M.Medvedkov<sup>5</sup>,  
G.I.Merzon<sup>9</sup>, R.A.Mukhamedshin<sup>6</sup>, V.A.Ryabov<sup>9</sup>, A.A.Semak<sup>10</sup>, V.A.Smotryaev<sup>7</sup>,  
S.V.Somov<sup>10</sup>, V.O.Tikhomirov<sup>9</sup>, I.S.Trostin<sup>7</sup>, V.A.Tsarev<sup>9</sup>, G.T.Zatsepin<sup>6</sup>

<sup>1</sup>*Dip. di Fisica dell'Università di Bari and INFN Sez. di Bari - Italy*

<sup>2</sup>*Dip. Fisica dell' Università di Bologna and INFN Sez. di Bologna - Italy*

<sup>3</sup>*INFN, Laboratori Nazionali del Gran Sasso, Assergi - Italy*

<sup>4</sup>*Dip. Fisica dell' Università di Lecce and INFN Sez. di Lecce - Italy*

<sup>5</sup>*Institute for High Energy Physics, Moscow - Russia*

<sup>6</sup>*Institute of Nuclear Research, Russian Academy of Science, Moscow - Russia*

<sup>7</sup>*Institute of Theoretical and Experimental Physics, Moscow - Russia*

<sup>8</sup>*Joint Institute for Nuclear Research, Moscow - Russia*

<sup>9</sup>*P.N.Lebedev Physical Institute, Moscow - Russia*

<sup>10</sup>*Moscow Engineering Physical Institute, Moscow - Russia*

<sup>11</sup>*Dip.di Scienze Fisiche Università di Napoli and INFN Sez. di Napoli - Italy*

<sup>12</sup>*Dip. Fisica dell' Università di Roma and INFN Sez. di Roma - Italy*

<sup>13</sup>*Dip. Fisica dell' Università di Roma III - Italy*

\* *Contact person*

# Introduction

The purpose of this document is to present the long baseline experiment ( $NOE$ ) at the Gran Sasso Laboratory for the measurement of neutrino masses looking for  $\nu_\mu \rightarrow \nu_\tau$  and  $\nu_\mu \rightarrow \nu_e$  oscillations. The first version of the  $NOE$  proposal has been submitted to the Gran Sasso Scientific Committee in February 1996. This progress report completes the detector study and technical design phase in which the Collaboration has performed tests and simulations to define the main parameters of the  $NOE$  hardware elements for the best achievement of the physics goals. The research program has to be fulfilled at minimum cost and taking into account safety requirements.

The philosophy of this design is to have oscillation sensitivity in two separate ways: by measuring a deficit of muons in apparent NC/CC ratio and by looking for the  $\tau$  decay in  $\nu_\mu \rightarrow \nu_\tau$  or for an electron excess in  $\nu_\mu \rightarrow \nu_e$ .

The major experimental hint for the long baseline  $\nu$  oscillation search in the regime of low  $\Delta m^2$  ( $10^{-2} \div 10^{-3}$  eV<sup>2</sup>) comes from the muon deficit observed by the Kamiokande and IMB experiments. At present the new SuperKamiokande experiment confirms the observed effect in Kamiokande data. Recent results from CHOOZ, a long baseline reactor neutrino experiment, show no evidence for neutrino oscillation in  $\bar{\nu}_e$  disappearance mode, up to  $\sin^2 2\theta > 0.18$  for large  $\Delta m^2$ .

Given the SuperKamiokande confirmation of the atmospheric neutrino anomaly and the negative CHOOZ result, a Long BaseLine (LBL) experiment has to fulfill the following requirements:

1. **The measurement of the parameter NC/CC.** This robust and unambiguous test is mandatory to investigate on the existence of a neutrino oscillation signal in LBL experiments. Moreover in a scenario, never ruled out, in which a neutrino oscillates with large mixing angle and  $\Delta m^2 \simeq 10^{-2} \div 10^{-3}$  eV<sup>2</sup> in a sterile neutrino ( $\nu_\mu \rightarrow \nu_x$ ) the oscillation can be discovered only by measuring near and far  $\nu_\mu$ CC spectra. There is no doubt that this measurement can be done only with a massive detector.
2.  **$\nu_\tau$  tagging.** If the oscillation signal is seen by measuring NC/CC ratio, the search for  $\nu_\tau$  appearance becomes a very important task. This search requires high detector performances.

The appearance of  $\tau$ 's can be definitively detected in  $NOE$  by observing a signal in several channels, each one corresponding to a different  $\tau$  decay. The detection of oscillated events with the appearance method and the  $\mu$ -deficit obtained studying the NC/CC ratio will allow a redundant oscillation signal measurement.

3. **Atmospheric neutrinos.** After the SuperKamiokande results, which suggest a possible shift of  $\Delta m^2$  to smaller values, the interest for the atmospheric neutrinos is raised up. It would be interesting, for a LBL experiment to test this effect using a

massive detector based on a different technique with respect to the water Čerenkov detectors.

4. **Fast response.** If a beam from CERN to Gran Sasso will be available in the next years, a strong competition with American and Japanese experimental LBL programs is foreseen: at present, the 7 kton  $NOE$  project can adequately compete with the 8 kton MINOS detector and with K2K.

According to the present oscillation scenario, the  $NOE$  research program can be summarized in this way:

- Inclusive (NC/CC)  $\nu_\mu$  disappearance and direct  $\nu_\tau$  appearance by kinematical tau decay reconstruction.
- Investigation of  $\nu_\mu \rightarrow \nu_e$  oscillation in a mixing angle region two orders of magnitude beyond the CHOOZ limit.
- Atmospheric neutrino studies.

Many efforts have been done to obtain a deeper understanding of the  $NOE$  detector, in terms of performances, granularity and cost in order to achieve the described physics goals.

The recent  $NOE$  evolution towards a more sophisticated layout devoted to  $\nu_\tau$  appearance is presented in detail in this progress report. In order to improve the  $\nu_\tau$  search, the apparatus has been implemented with Transition Radiation Detector (TRD) interleaved between calorimetric modules (CAL). The combination of TRD and CAL information strongly enforces  $e$ ,  $\mu$ , and  $\pi$  identification, thus opening, besides  $\tau \rightarrow \mu$ , new tau decay channels:  $\tau \rightarrow \pi$  and  $\tau \rightarrow e$  with very clean signatures. The last one is particularly favoured due to the low background (residual  $\nu_e$  beam). The good electron identification in the TRD target and the low  $\pi^0$  background allow to obtain high  $\sin^2 2\theta$  sensitivity in the  $\nu_\mu \rightarrow \nu_e$  oscillation channel, thus considerably enlarging the region investigated by the CHOOZ reactor experiment.

In the present report both TRD and CAL will be extensively discussed. The TRD is an evolution of that now operating in the MACRO detector at Gran Sasso. The performances of this kind of detector are well known and the technique is largely proven. In order to contain the cost of the calorimeter as much as possible, different options have been examined and the performances compared as well. The project is still in progress, in particular as far as the electronic read out, trigger, data acquisition and detector optimization are concerned. It should be stressed that this massive detector is based on proven technology which guarantees complementarity to the approved ICARUS experiment.

In conclusion, the present progress report will focus on the new design of the  $NOE$  long baseline detector and its capability to explore the oscillating neutrino physics.

# Chapter 1

## Physical motivations

### 1.1 Introduction

One of the open and most debated problems in elementary particle physics is whether neutrinos are massless or not. Very small neutrino masses are unlikely to be measured via the classical  $\beta$ -decay procedure. If neutrinos have non zero mass and the mass eigenstates are mixed, the most promising way to measure their mass is through oscillation experiments, as foreseen by Bruno Pontecorvo.

In the simplified hypothesis of a mixing between two neutrino families, the probability of observing  $\nu_i \rightarrow \nu_j$  oscillations is given by

$$P(\nu_i \rightarrow \nu_j) = \sin^2 2\theta \sin^2 \left[ \frac{1.27 \Delta m^2 L}{E_\nu} \right] \quad (1.1)$$

where  $\Delta m^2 = m_i^2 - m_j^2$  is in  $\text{eV}^2$ ,  $L$  is the distance from the  $\nu$  source to the detector in km and  $E_\nu$  is the neutrino energy in GeV.

For maximal mixing, this probability is different from zero if  $\Delta m^2$  is at least of the order of  $E_\nu/L$ . Solar neutrino data ( $E_\nu \sim \text{few MeV}$ ,  $L = 150 \cdot 10^6 \text{ km}$ ) cover  $\Delta m^2$  regions from  $10^{-5}$  to  $10^{-10} \text{ eV}^2$  and existing accelerator experiments can go up to  $\Delta m^2 \sim 1 \text{ eV}^2$ . The region of  $\Delta m^2 = 10^{-2} \div 10^{-3} \text{ eV}^2$  can be covered with long baseline  $\nu_\mu$ -beams (average energy  $\sim 10 \div 15 \text{ GeV}$ ,  $L \sim 10^3 \text{ km}$ ) and overlaps with the region of atmospheric neutrinos ( $E_\nu \sim 1 \text{ GeV}$ ,  $L = 10 \div 10^4 \text{ km}$ ). Long baseline neutrino beams provide a very clean way to study  $\nu_\mu$  oscillations at small  $\Delta m^2$  values, offering several advantages when compared with atmospheric neutrinos (high flux, known energy spectrum, known initial neutrino direction and flavor and  $\nu_e$  contamination).

A muon neutrino beam peaked around an energy of several GeV can be used to detect  $\tau$  neutrino appearance via  $\nu_\tau$  CC interactions. Long baseline projects are being proposed in various laboratories in the world (Fermilab to Soudan, CERN to Gran Sasso, KEK to SuperKamiokande) and are at different stages of approval. In addition, a LBL detector with good tracking and energy resolution could be also sensitive to the atmospheric neutrinos in the region of  $L/E = 10^3 \div 10^4 \text{ (km/GeV)}$ . This oscillation search would be complementary to that performed with LBL neutrino beam. The combination

of both measurements allows to extend the sensitivity of the detector in the region of  $\Delta m^2 = 10^{-2} \div 10^{-4} \text{ eV}^2$ .

## 1.2 Hints from atmospheric neutrinos

Atmospheric electron and muon neutrinos are decay products of mesons created by cosmic ray interactions in the atmosphere. They are usually detected in large underground detectors. The flux in the few-GeV range has been measured looking at interactions inside massive target detectors (the so-called contained or partially contained events). In the 100-GeV range the  $\nu_\mu$  flux is deduced by detecting upward-travelling muons produced by  $\nu$ 's in the rock below the apparatus. The  $\nu$ -pathlength is estimated looking at the direction of the produced particles ( $e$  or  $\mu$ ) and it ranges from  $\sim 20$  km to  $\sim 12000$  km.

Because of the values of energy  $E_\nu$  and pathlength  $L$ , the atmospheric neutrino data cover the wide range  $1 > E_\nu/L > 10^{-4}$  (GeV/km). Thus the measurement of the neutrino flux and its angular shape result crucial in order to verify the oscillation hypothesis.

In order to reduce the effect of theoretical uncertainties on the  $\nu$ -fluxes, the double ratio is often considered:

$$R = \frac{(\mu/e)_{data}}{(\mu/e)_{MC}}, \quad (1.2)$$

where  $(\mu/e)_{data}$  is the measured ratio of muon to electron neutrino interactions in the detector and  $(\mu/e)_{MC}$  is the expected one, assuming no oscillations.

A strong indication for an atmospheric neutrino anomaly comes from the Kamiokande [1] and IMB [2] water Čerenkov detectors, which measured values of  $R$  significantly lower than 1. These results were confirmed by the Soudan tracking detector [3], while two other tracking experiments (Frejus [4] and Nussex [5]) reported no effect.

The best fit of data indicates, as most probable, maximum mixing ( $\sin^2 2\theta \sim 1$ ) and a neutrino mass difference  $\Delta m^2$  of the order of  $10^{-2} \text{ eV}^2$ .

The first preliminary results of the new detector SuperKamiokande [6, 7] for the double ratio confirm with higher statistics the atmospheric neutrino anomaly and indicate lower values of  $\Delta m^2$ . The oscillation parameter area compatible with Kamiokande and also with SuperKamiokande measurements is centered around  $\sin^2 2\theta \sim 1$  and  $\Delta m^2 \sim 5 \cdot 10^{-3} \text{ eV}^2$ .

An independent measurement of neutrino-induced upward-going muon flux has been made by the MACRO experiment resulting in a deficit of  $\nu_\mu$  [8]. The agreement between measured and expected flux improves assuming the oscillation parameter values suggested by the Čerenkov experiments.

These results of the atmospheric neutrino measurements indicate maximum mixing and an upper limit on  $\Delta m^2$  of about  $10^{-2} \text{ eV}^2$  and suggest to investigate carefully the option of proper energy neutrino beam for the long baseline experiments.

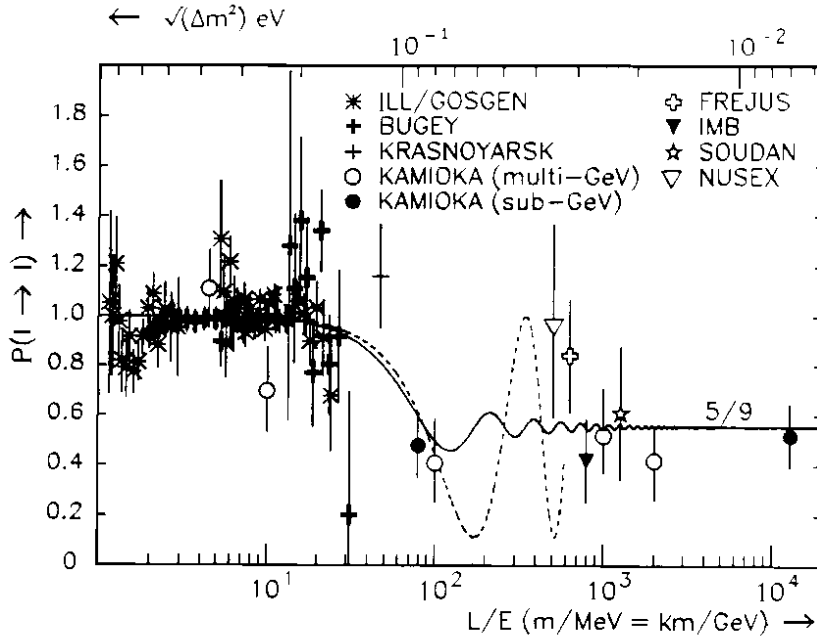


Figure 1.1: The first threshold of the oscillation curve and disappearance rates as a function of  $L/E$ .

### 1.3 Three-Flavor Mixing

Harrison, Perkins and Scott [9] have pointed out that atmospheric and solar neutrino data could be explained in a threefold maximal mixing scheme assuming two independent mass-squared differences :  $\Delta m^2 = (0.72 \pm 0.18) \cdot 10^{-2} \text{ eV}^2$  and  $\Delta m^2 < 0.9 \cdot 10^{-11} \text{ eV}^2$ . For  $L/E < 1/\Delta m^2$  the flavor survival probability formula returns  $P(\nu_l \rightarrow \nu_l) = 1$ , while for  $L/E > 1/\Delta m^2$  the value of this quantity, averaged over the neutrino spectrum, is expected to be  $5/9$ . The two plateau regions are separated by a well localized threshold at  $L/E \sim 1/\Delta m^2$ . The corresponding appearance probability  $P(\nu_l \rightarrow \nu_{l'})$  to produce a neutrino of different flavor  $l' \neq l$  is equal to  $2/9$  sharing the oscillation between  $\nu_\mu \rightarrow \nu_e$  and  $\nu_\mu \rightarrow \nu_\tau$  channels. A similar threshold at  $L/E \sim 1/\Delta m^2$  gives rise to a third plateau characterized by a survival probability equal to  $1/3$ . The data from all the experiments are shown in Fig. 1.1 as a function of  $L/E$  : they suggest the existence of a sharp threshold in the region  $L/E = 20 \div 80 \text{ km/GeV}$  corresponding to  $\Delta m^2 \sim 10^{-2} \text{ eV}^2$ .

Beyond this threshold the data suggest a plateau close to the prediction  $P(\nu_l \rightarrow \nu_l) = 5/9 \simeq 0.56$ , characteristic of maximal mixing. The atmospheric anomaly could be explained in this way. The figure also shows the full oscillation curve corresponding to  $\Delta m^2 = 0.72 \cdot 10^{-2} \text{ eV}^2$  under a maximal mixing hypothesis.

A minimum is expected for  $L/E = 170 \text{ km/GeV}$ . Given  $L$  and measured  $E$  one could map out the energy dependence both for the disappearance and the appearance rates  $\nu_\mu \rightarrow \nu_e$  and/or  $\nu_\mu \rightarrow \nu_\tau$  providing the first detailed proof of the neutrino oscillation existence.

At the moment, first results from the CHOOZ experiment [10], showing no evidence for neutrino oscillation in the  $\bar{\nu}_e$  disappearance channel, seem to rule out the present 3-flavour



maximal mixing theoretical solution of the neutrino oscillations. Nevertheless, having the SuperKamiokande data confirmed a  $\nu_\mu$  atmospheric deficit, the neutrino oscillation problem remains still open, making  $\nu_\mu \rightarrow \nu_\tau$  a possible explanation of that anomaly.

Both the oscillation and the  $\nu_\tau$  discovery are important tests of the Standard Model in elementary particle physics. The forthcoming LBL program at Gran Sasso, K2K and Soudan are the best sites for  $\nu_\tau$  appearance search.

For a clean and redundant  $\nu_\tau$  evidence, a LBL detector has to be able to perform both inclusive (NC/CC, disappearance) and exclusive (appearance) searches. The proposed 7 kton  $N^{\mathcal{O}E}$  detector is massive enough to measure a NC/CC anomalous ratio, the most simple and fast method to recognize neutrino oscillations. Besides, the detector can measure kinematical  $\nu_\tau$  appearance by looking at 3 different  $\tau$  decay channels,  $\tau \rightarrow \mu$ ,  $\tau \rightarrow e$ ,  $\tau \rightarrow \pi$ , for a total branching ratio of about 50 %.

# Chapter 2

## The CERN - Gran Sasso LBL project

### 2.1 The neutrino beam

The feasibility of a  $\nu_\mu$  beam from CERN to LNGS has been considered in the framework of the LHC project [11]. New transfer lines are required in order to bring the SPS to LHC. In the project it is proposed to derive the primary proton beam from one of these lines; this beam may be deflected and directed to Gran Sasso in a 550 m transfer line, followed by a target and a focusing station (25 m).

The decay of pions and kaons produces essentially  $\mu$ 's and  $\nu_\mu$ 's. Hence it is possible to generate a neutrino beam starting from the decay of secondaries (charged  $\pi$  and  $K$ ) produced by the interactions of a primary proton beam on a target. The secondary particles are focused towards a detector and left to decay in a vacuum tunnel. A beam dump at the end of the tunnel stops muons and all remaining hadrons. It is important to remind that a small contamination of  $\nu_e$  is unavoidably present in the neutrino beam, due to  $\pi$ ,  $K$  and muon decay. The decay tunnel is going to be 1 km long, with a diameter of a few meters. Table 2.1 shows absolute and relative coordinates for the two sites.

The  $\nu$ -beam from CERN to LNGS will enter the present underground halls with an angle of  $93.3^\circ$  with respect to gallery axis. The project foresees two different extraction

Site	$\lambda$	$\phi$	$\Lambda$	$\alpha$	Distance
CERN	$6.073^\circ$	$46.24^\circ$			
LNGS	$13.57^\circ$	$42.45^\circ$	$122.5^\circ$	$3.283^\circ$	731 km

Table 2.1: Absolute coordinates  $(\lambda, \phi)$  and azimuth and declination angles  $(\Lambda, \alpha)$  of the direction Gran Sasso-CERN.

Operating mode	Energy (GeV)	Cycle length (s)	Proton on target per cycle	Proton on target per run
dedicated	450	7.2	$3 \times 0.8 \times 10^{13}$	$2.0 \times 10^{19}$
shared	450	14.4	$2 \times 0.9 \times 10^{13}$	$0.75 \times 10^{19}$

Table 2.2: Performances of the SPS machine for dedicated and shared mode.

Focusing	Events/ $10^{19}$ pot/kton	$\langle E_\nu^{-2} \rangle^{-1/2}$ (GeV)	$\nu_e/\nu_\mu$ (%)
H20R40 [12]	473	10.5	1.4
H40R70 [12]	722	14.2	1.1
Single horn [13]	1040	22.8	0.65

Table 2.3: Event rates, neutrino mean energy and  $\nu_e$  contamination for a 450 GeV/c proton beam, a flux of  $10^{19}$  protons on target and a fully efficient detector at Gran Sasso.

cycles. During the LHC construction it is possible to have a neutrino beam dedicated cycle of 7.2 s with 3 fast extractions of 6  $\mu$ s at a 50 ms interval.

When LHC will be operating, the beam has to be shared among different projects. Then, only a cycle of 14.4 s with 2 fast extractions of 10  $\mu$ s at 50 ms interval for the neutrino beam will be used. Table 2.2 shows the performance of the machine in these two cases.

The total number of protons on target is given for a run of 100 days ( $10^7$  s) at 70 % efficiency, which corresponds to about one year of operation. At present SPS is working in shared mode. Two detailed simulations of the transport beam and of the decay of secondaries have been carried out independently [12, 13, 14]. For the production target both simulations assume the same configuration now used for the short baseline at CERN, i.e. a segmented beryllium rod (1.2 m long, with a radius of 1.5 mm). Moreover the target is compatible with fluxes lower than  $1.5 \cdot 10^{13}$  protons per fast extraction; other types of target are under study for higher fluxes. Several possibilities have been analyzed for magnetic lenses: a horn-reflector system and different configurations of the magnets, tuned to focalize different monochromatic beams. Results of the simulations are reported in Table 2.3. Event rates, neutrino mean energy and  $\nu_e$  contamination are reported assuming a 450 GeV/c primary beam energy and two different focusing systems.

In Fig. 2.1 the neutrino energy for CC interactions is shown for the different cases. In Fig. 2.2 the radial distribution of the  $\nu$  beam at Gran Sasso is shown.

Recently a different SPS operating mode [15] has been proposed, with a 19.2 s super-cycle. An increase in the proton flux of a factor 2 to 4 with respect to the shared mode of Table 2.2 appears to be possible.

The choice of neutrino beam energy is open : recent results on atmospheric neutrinos (see §1.2) suggest that, at the Gran Sasso location, the oscillation probability is maximum at few GeV. Fig. 2.3 shows the oscillation probability at Gran Sasso as a function of neutrino energy for different  $\Delta m^2$  values. Therefore a low energy beam seems to be

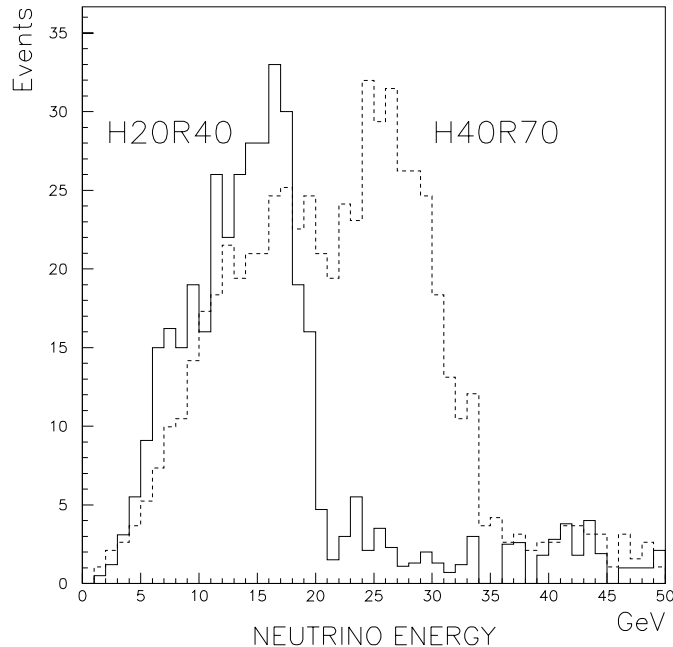


Figure 2.1:  $\nu_\mu$  energy distributions for CC interactions. The number of events is given for a 1 kton detector operating 1 year at Gran Sasso.

preferable.

## 2.2 Oscillation signatures

### 2.2.1 Oscillating event rates

As it has been stated in §1.3 the most important issue is the measurement of the  $\nu$ -survival probability and its complementary probability of different  $\nu$ -flavors appearance. These measurements can be performed by looking at the depletion of  $\nu_\mu$  CC events and at the appearance of  $\nu_e$  CC (and/or  $\nu_\tau$  CC) as a function of  $L/E$ . In particular at Gran Sasso,  $L = 731$  km away from CERN, in the hypothesis of oscillation parameters suggested by the atmospheric anomaly (see curve for  $\Delta m^2 = 5 \cdot 10^{-3} eV^2$  in Fig. 2.3), the energy spectrum of the  $\nu_\mu$ -beam described in §2.1 seems to be well suited for this kind of measurement. The first full oscillation cycle will be more evident if the event energy is well measured.

In the following sections, the response to a large mixing atmospheric signal of a general  $NOE$  like 7 kton detector at the Gran Sasso Laboratory, is reported. In order to take into account the muon identification capability of the detector in deep inelastic interactions, a cut on the reconstructed  $\mu$  energy has been considered ( $E \geq 1$  GeV).

Two different detector configurations have been considered:

1. an ideal detector with infinite resolution.
2. a  $NOE$  like detector with a  $40\%/\sqrt{E}$  resolution.

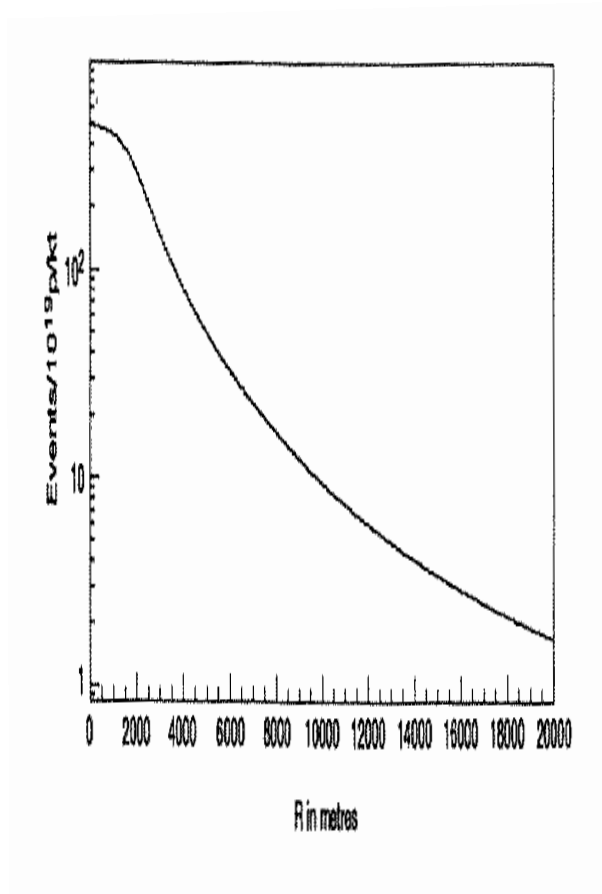


Figure 2.2:  $\nu_\mu$  beam radial distribution at Gran Sasso.

Given an exposure of  $1.5 \cdot 10^{20}$  protons on target with a neutrino energy of 15 Gev [12] and taking into account the arguments of §2.1,  $N^{OE}$  is expected to detect  $\sim 4 \cdot 10^4$   $\nu_\mu$  CC unoscillated events in  $3 \div 4$  years of operation. At present this number of events seems reasonably conservative. In absence of oscillations, Fig. 2.4 shows the expected energy distribution of the reconstructed simulated  $\nu_\mu$  CC events assuming the two detector resolutions.

In case of oscillations, a  $N^{OE}$  -like detector will be able to measure:

- $\nu_\mu$  disappearance as a function of the energy, by collecting  $\nu_\mu$  CC interaction events.
- excess of  $\nu_e$  CC and/or  $\nu_\tau$  CC interactions respectively for  $\nu_\mu \rightarrow \nu_e$  and/or  $\nu_\mu \rightarrow \nu_\tau$  oscillations.

Finally, in the atmospheric neutrino measurement, when the distance between source and detector is known, a good energy resolution on the reconstructed neutrino event could allow to plot  $\nu_\mu$  disappearance distribution as a function of  $L/E$ .

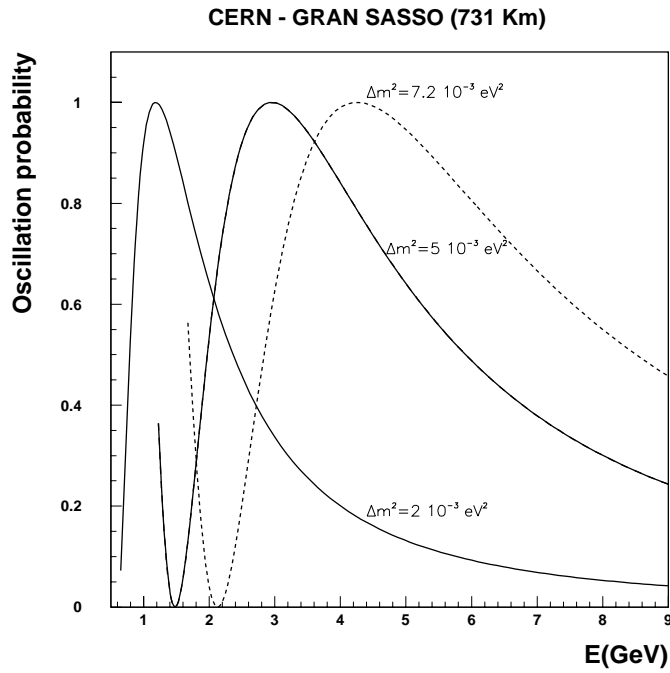


Figure 2.3: Oscillation probability dependence on neutrino energy ( $\sin^2 2\theta=1$ ).

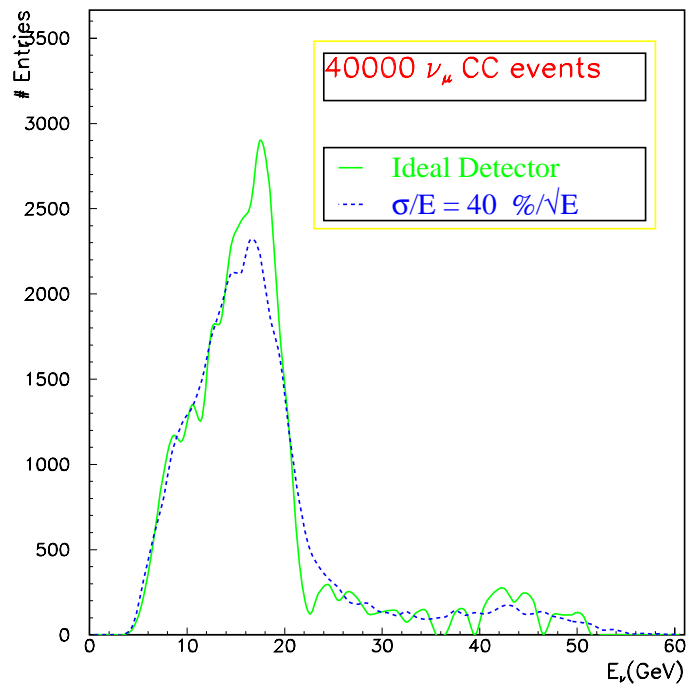


Figure 2.4:  $\nu_\mu$  CC interaction spectrum.

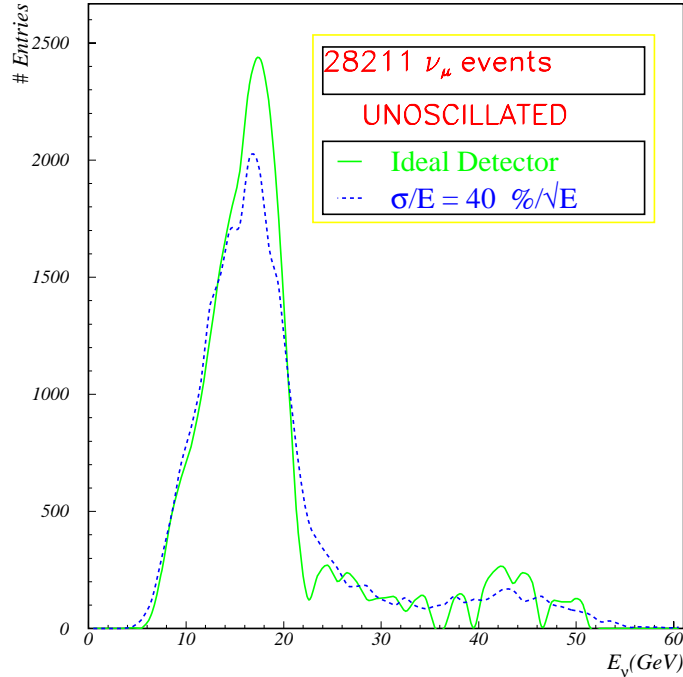


Figure 2.5: Residual  $\nu_\mu$  CC interaction spectrum at Gran Sasso location for  $\Delta m^2 = 7.2 \cdot 10^{-3} \text{ eV}^2$ .

### 2.2.2 $\nu_\mu$ disappearance

If  $\nu_\mu$  oscillations exist, the rate of  $\nu_\mu$  CC interactions will be depleted independently of the flavor in which the neutrino has oscillated (Fig. 2.5).

According to the hypothesis of  $\Delta m^2 = 7.2 \cdot 10^{-3} \text{ eV}^2$  (value suggested in [9]) and maximal mixing, a survival curve as a function of the energy can be drawn dividing residual  $\nu_\mu$  CC by total  $\nu_\mu$  CC (Fig. 2.6).

In Fig. 2.7 the survival probability assuming  $\Delta m^2 = 7.2 \cdot 10^{-3} \text{ eV}^2$  is shown for different mixing values. In Fig. 2.8 the same probability is shown assuming  $\Delta m^2 = 5 \cdot 10^{-3} \text{ eV}^2$  (SuperKamiokande test value).

### 2.2.3 $\nu_\tau$ and $\nu_e$ appearance

Once the  $\nu_\mu$  flux has been found depleted, the next step will be the understanding of the nature of the oscillation. In principle both neutrino flavors ( $\nu_e, \nu_\tau$ ) are likely, hence the detector must be able to discriminate them unambiguously through their charge current interactions. Maximal transition rates in  $\nu_e$  or  $\nu_\tau$  are considered in the present calculation. If oscillations to  $\nu_e$  and  $\nu_\tau$  are not equally likely, the respective  $\nu_\mu \rightarrow \nu_e$  and  $\nu_\mu \rightarrow \nu_\tau$  rates can be easily deduced. In the hypothesis of a predominant  $\nu_\mu \rightarrow \nu_e$  mixing, the oscillating  $\nu_e$  CC and the residual  $\nu_\mu$  CC will be respectively 11789 and 28211 events while the energy spectra are shown in Figs 2.9 and 2.5. Conversely  $\nu_\tau$  CC events are depleted by a cross section ratio  $\eta \sim \sigma_\tau/\sigma_\mu$ , that suppresses the  $\tau$  generation. The number of the oscillated  $\nu_\tau$  CC as a function of energy is shown in Fig. 2.10. Moreover the branching ratio of tau decaying into leptonic channels leads to 674  $\tau \rightarrow \mu$  and 674  $\tau \rightarrow e$  collected in the

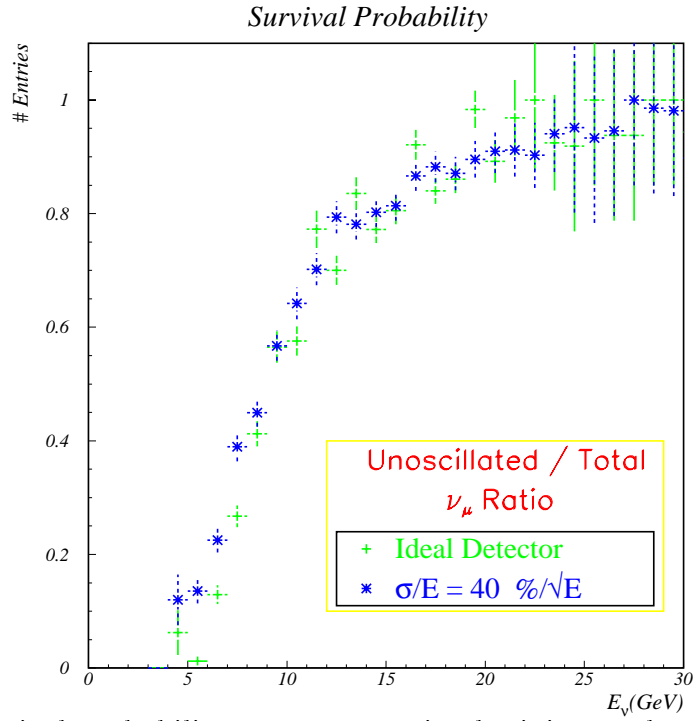


Figure 2.6:  $\nu_\mu$  survival probability curve at maximal mixing angle and for  $\Delta m^2 = 7.2 \cdot 10^{-3} eV^2$ .

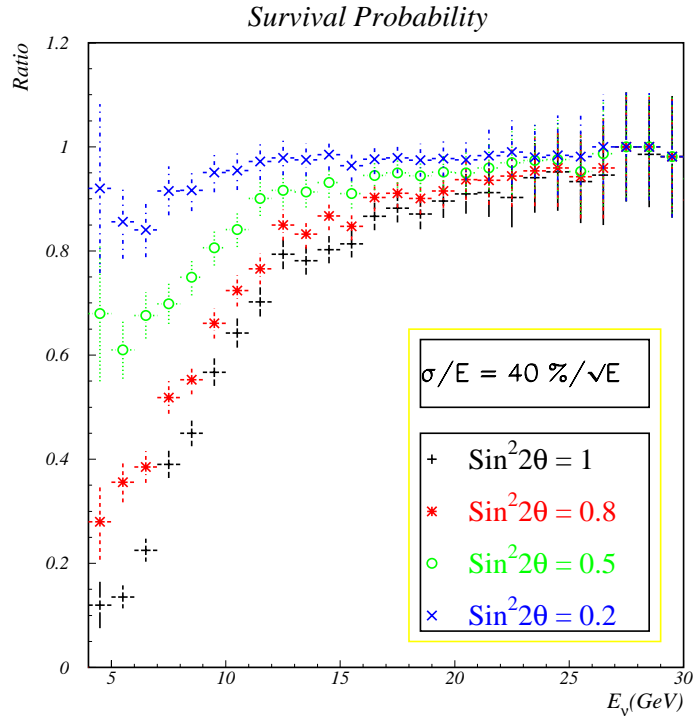


Figure 2.7:  $\nu_\mu$  survival probability at different mixing angles with  $\Delta m^2 = 7.2 \cdot 10^{-3} eV^2$ .



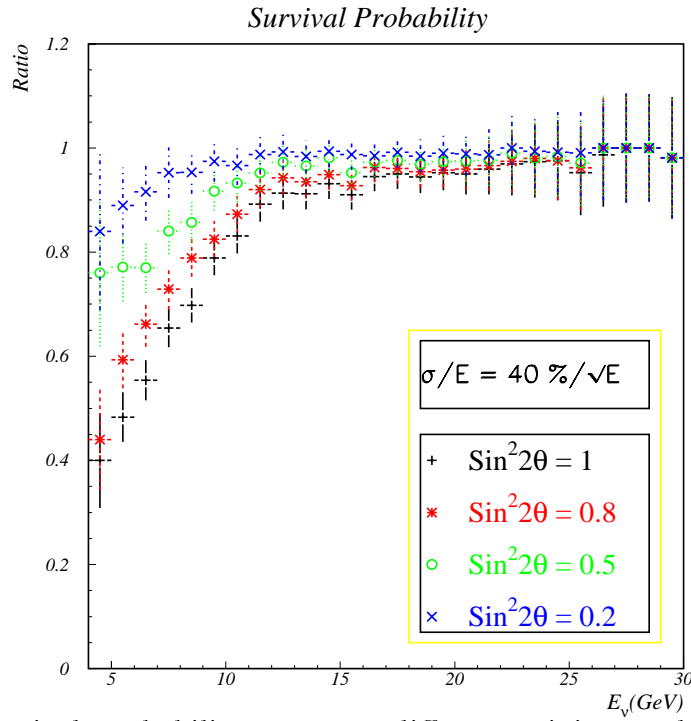


Figure 2.8:  $\nu_\mu$  survival probability curve at different mixing angles with  $\Delta m^2 = 5 \cdot 10^{-3} \text{ eV}^2$ .

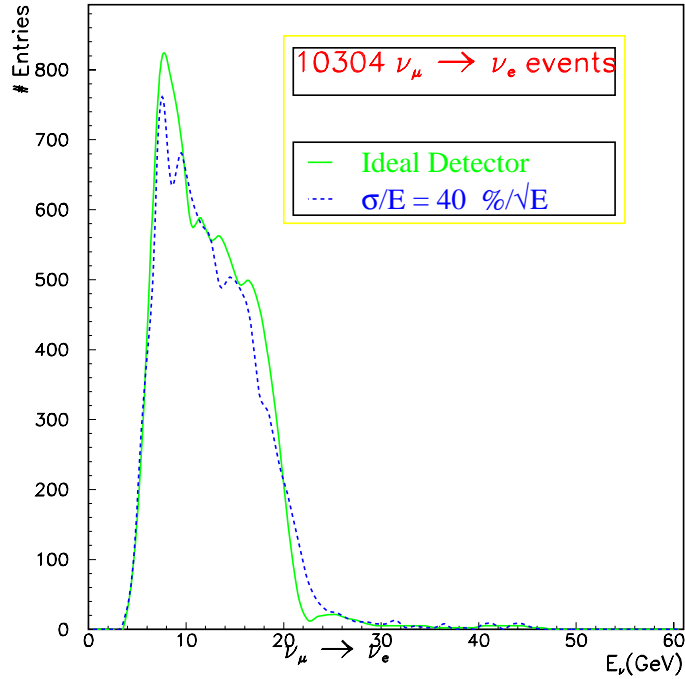


Figure 2.9:  $\nu_e$  CC interactions for  $\Delta m^2 = 7.2 \cdot 10^{-3} \text{ eV}^2$  and maximal mixing.

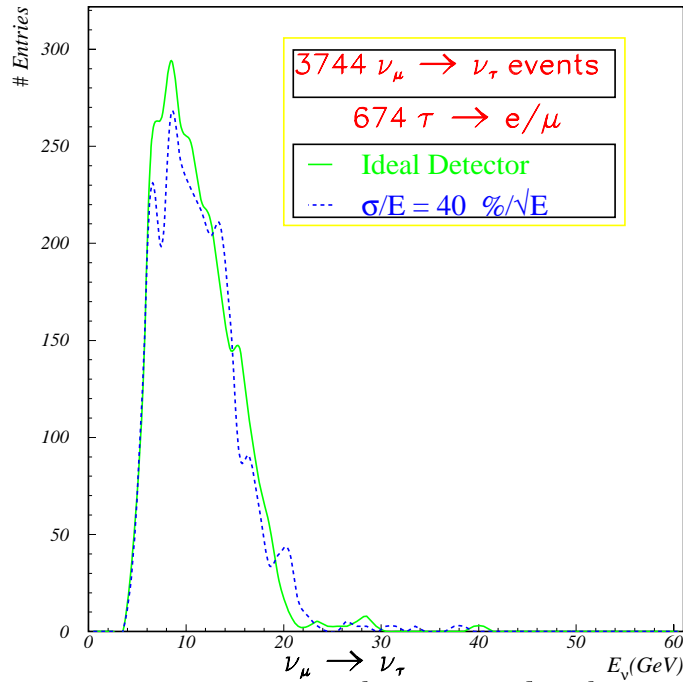


Figure 2.10:  $\nu_\tau$  CC interactions for  $\Delta m^2 = 7.2 \cdot 10^{-3} \text{ eV}^2$  and maximal mixing.

same exposure conditions described in last section. In spite of these depletion factors the oscillation effect is still large and unambiguous.

Tables 2.4, 2.5 and 2.6 summarize the expected numbers of events at Gran Sasso with and without oscillation. The used values are  $\Delta m^2 = 7.2 \cdot 10^{-3} \text{ eV}^2$  and  $\Delta m^2 = 5 \cdot 10^{-3} \text{ eV}^2$  respectively.

Both in  $\nu_\mu \rightarrow \nu_\tau$  and  $\nu_\mu \rightarrow \nu_e$  oscillation cases, a shift of the energy spectrum towards lower energy is clearly visible. Therefore a change in the energy spectrum shape could be a further oscillation test.

**No Oscillation**

Processes	# of Events
$\nu_\mu$ CC DIS	34963
$\nu_\mu$ CC Q.E.	2239
$\nu_\mu$ CC RES.	2798
$\nu_e$ CC DIS. beam contamination	350
$\nu_e$ CC Q.E. beam contamination	22
$\nu_e$ CC RES. beam contamination	28

Table 2.4: Expected Number of events at the Gran Sasso site without oscillation. (DIS= Deep Inelastic Scattering, Q.E.= Quasi Elastic scattering, RES.= Baryon Resonance production).

**Oscillations ( $\Delta m^2 = 7.2 \cdot 10^{-3} \text{ eV}^2$ )**

Processes	# of Events
$\nu_\mu$ CC DIS (residual)	24659
$\nu_\mu$ CC Q.E. (residual)	1579
$\nu_\mu$ CC RES. (residual)	1973
$\nu_\mu \rightarrow \nu_e$ CC DIS	10304
$\nu_\mu \rightarrow \nu_e$ CC Q.E.	660
$\nu_\mu \rightarrow \nu_e$ CC RES.	825
$\nu_\mu \rightarrow \nu_\tau$ CC DIS	3744
(Branching Ratio $\tau \rightarrow \mu$ )	674
(Branching Ratio $\tau \rightarrow e$ )	674
(Branching Ratio $\tau \rightarrow \pi$ )	517
$\nu_\mu \rightarrow \nu_\tau$ CC Q.E.	265
(Branching Ratio $\tau \rightarrow \mu$ )	48
(Branching Ratio $\tau \rightarrow e$ )	48
(Branching Ratio $\tau \rightarrow \pi$ )	37
$\nu_\mu \rightarrow \nu_\tau$ CC RES.	294
(Branching Ratio $\tau \rightarrow \mu$ )	53
(Branching Ratio $\tau \rightarrow e$ )	53
(Branching Ratio $\tau \rightarrow \pi$ )	40

Table 2.5: Expected Number of events at the Gran Sasso site with oscillation. Used parameters are  $\Delta m^2 = 7.2 \cdot 10^{-3} \text{ eV}^2$ ,  $\sin^2 2\theta = 1$  (max mixing). (DIS=Deep Inelastic Scattering, Q.E.= Quasi Elastic scattering, RES.= baryon Resonance production).

**Oscillations** (  $\Delta m^2 = 5 \cdot 10^{-3} \text{ eV}^2$  )

Processes	# of Events
$\nu_\mu$ CC DIS (residual)	28571
$\nu_\mu$ CC Q.E. (residual)	1830
$\nu_\mu$ CC RES. (residual)	2286
$\nu_\mu \rightarrow \nu_e$ CC DIS	6392
$\nu_\mu \rightarrow \nu_e$ CC Q.E.	410
$\nu_\mu \rightarrow \nu_e$ CC RES.	511
$\nu_\mu \rightarrow \nu_\tau$ CC DIS	1910
(Branching Ratio $\tau \rightarrow \mu$ )	343
(Branching Ratio $\tau \rightarrow e$ )	343
(Branching Ratio $\tau \rightarrow \pi$ )	229
$\nu_\mu \rightarrow \nu_\tau$ CC Q.E.	135
(Branching Ratio $\tau \rightarrow \mu$ )	24
(Branching Ratio $\tau \rightarrow e$ )	24
(Branching Ratio $\tau \rightarrow \pi$ )	16
$\nu_\mu \rightarrow \nu_\tau$ CC RES.	150
(Branching Ratio $\tau \rightarrow \mu$ )	27
(Branching Ratio $\tau \rightarrow e$ )	27
(Branching Ratio $\tau \rightarrow \pi$ )	18

Table 2.6: Expected Number of events at the Gran Sasso site with oscillation. Used parameters are  $\Delta m^2 = 5 \cdot 10^{-3} \text{ eV}^2$ ,  $\sin^2 2\theta = 1$  (max mixing). (DIS= Deep Inelastic Scattering, Q.E.= Quasi Elastic scattering, RES.= baryon Resonance production).

# Chapter 3

## Experimental setup

### 3.1 Detector design

The low  $\nu$ -beam luminosity at long distance (beam luminosity decreases as  $1/L^2$ ) implies that a long baseline detector must be very massive and have a diffuse target. Unlike the case of short baseline experiments these constraints imply a detector in where parts should be, at the same time, target, tracker, calorimeter, and  $\mu$ -detector.

Oscillation tests can be grouped in two classes:

1. Inclusive measurements:

- $\nu_\mu$  disappearance: comparing the fluxes measured near the accelerator and in the far detector, the presence of a  $\mu$ -deficit at long distance can be tested.
- Measurement of the ratio of events without muon track (appearing NC events) with respect to those with a muon track (appearing  $\nu_\mu$  CC events).

2. Exclusive measurements:

- Search for  $\nu_\tau$  and/or  $\nu_e$  appearance. This analysis can be performed on an event by event basis, taking advantage of both the spatial and the topological event reconstruction. A detector devoted mainly to this measurement should have very high granularity as well as good particle identification capability. A beam monitor, identifying the residual  $\nu_e$  beam background, could be also very useful for this kind of analysis.

Inclusive measurements require only  $\mu$  identification in the detector and do not need event reconstruction. On the contrary, exclusive measurements require enough granularity to permit the separation between CC interactions with or without  $\tau$ 's in the final state when  $\nu_\mu \rightarrow \nu_\tau$  oscillation occurs. Such a discrimination is based on the measurement of the missing momentum in the plane orthogonal to the  $\nu$ -beam direction, on the angular correlation between missing momentum, outgoing lepton (pion) and hadronic jet

directions as well. In  $\nu_\tau$  CC interactions, the missing momentum is mainly due to the neutrino(s) coming out from tau decay.

In  $\nu_\mu \rightarrow \nu_e$  oscillation an excess of electrons will be looked for. Also in this oscillation channel the granularity allows to separate the genuine signal from NC with  $\pi^0$  events. Hence, general requirements for an adequate detector performing such exclusive measurements are the following:

- The mass in a large fiducial volume must be enough to contain the events inside the detector in order to have good sensitivity limits.
- $e, \mu, \pi^0, \pi^\pm$  discrimination.
- Fine topological readout to determine the shower axis and to allow electron - pion discrimination by the analysis of lateral and longitudinal shower profiles.
- Good kinematical reconstruction in terms of energy and angle of final prongs.

LBL experiments should be able to perform more than one oscillation test simultaneously. Moreover, when a large signal (atmospheric anomaly) is present, a detector with a good energy resolution can easily follow the oscillation modulation, as a function of L/E (E varying while L, the distance from the accelerator to the detector is fixed, see § 2.2).

A good compromise between mass and granularity allows to perform all these measurements.

## 3.2 The $N^{\text{OE}}$ Detector

According to the previous conceptual considerations, the essential elements of the  $N^{\text{OE}}$  detector are a massive, fine grain 4.3 kton calorimeter (CAL) interleaved with "lighter" Transition Radiation Detector (TRD) modules for a total TRD mass of 2.4 kton. Both TRD and CAL modules, joined together, form the Basic Module (BM) of the  $N^{\text{OE}}$  detector (Fig. 3.1). The whole 7 kton  $N^{\text{OE}}$  detector is made of twelve subsequent BM (Fig. 3.2).

Combining the information coming from both subdetectors (TRD and CAL) the discrimination between electrons, muons and pions is strongly improved, thus opening, besides  $\tau \rightarrow \mu\nu\nu$ , the study of other  $\tau$  decay channels. The TRD radiators, interleaved with multiple graphite layers, allow to measure quasi elastic events, reducing at a level as low as possible the nuclear reinteraction effects (§ 4.2).

Since the transition radiation is detected by many layers of proportional tubes, the muon energy can be determined by multiple measurements of the energy loss  $dE/dx$ , once a muon track is recognized in the calorimeter. The advantage of such a "distributed muon detector" is the capability to measure the muon energy even for muon tracks exiting the apparatus from the side walls, thus increasing the detector acceptance.

Based on the same principle, a muon catcher to measure the muon energy when the neutrino interaction occurs in the last TRD or CAL target, is placed at the end of the detector.

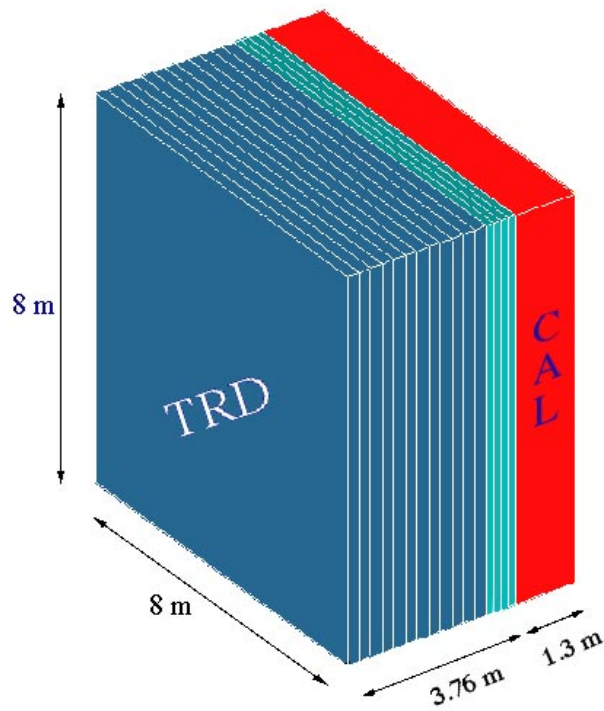


Figure 3.1: The Basic Module of the  $NOE$  detector

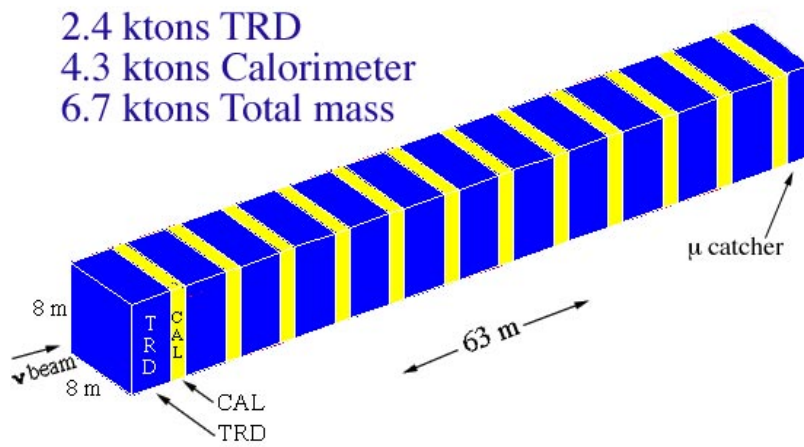


Figure 3.2: Schematic view of the  $NOE$  detector

In this report it is demonstrated that also in LBL experiments two subdetectors can be used, thus improving the detector performances. Particle identification in TRD and CAL, electron and hadron energy measurements in CAL and muon energy measurement in TRD, are the high quality features of this new and unique LBL detector. Background reduction is increased, allowing easy appearance oscillation signatures. In addition lighter TRD and heavier CAL detector-target, exploiting their different properties, can be addressed to independent classes of events, in particular recovering the quasi elastic and resonant interactions.

The contribution to the total cost of TRD and CAL subdetector has to be cleverly shared in order to keep the detector cost as low as possible. In general, for a given mass, this layout does not introduce any additional cost with respect to a single subdetector module (Table 5.1). Being the TRD technique well known and proven, the cost can be easily evaluated. A large volume TRD built for the MACRO detector has been extensively experimented at Gran Sasso, thus ensuring to the present collaboration the suitable expertise.

As far as the calorimeter is concerned, different designs have to be carefully examined, in order to compare cost and feasibility without losing the calorimetric performances.

### 3.3 The $N^{\text{OE}}$ TRD

The main task of the TRD subdetector (combined with CAL) is to provide a very clean electron identification, followed by an energy measurement in the calorimeter. Besides  $\nu_e$  appearance search, new  $\tau$  decay channels can be opened by looking at  $e$  and  $\pi$  tau decays. Due to the low electron background coming from the residual  $\nu_e$  beam (1%  $\nu_\mu$ ), the  $\tau \rightarrow e\nu\nu$  channel is particularly favoured. In fact, even without event reconstruction, the electron signal overcomes the background when the atmospheric parameters are considered.

A second fundamental task fulfilled by a TRD subdetector is the energy measurement of the muon generated in  $\nu_\mu\text{CC}$  and  $\nu_\tau\text{CC}$  interactions.

Since muon tracks cross many layers of TRD proportional tubes, the long pathlength in the gas allows to obtain the  $\mu$  energy, through multiple  $dE/dx$  measurements, with a resolution comparable to that achieved by using magnetic field technique. The described method is not expensive, it does not need electric power, magnetic coil and heat dissipation. It can benefit of the low cost TRD subdetector that, at the same time, is able to fulfill two important tasks:  $e$  and  $\pi$  identification (together with the calorimeter) and muon energy measurement.

#### 3.3.1 General description

The TRD module consists of 32 vertical layers of  $8 \times 8 \text{ m}^2$  surface area, each made of a polyethylene foam radiator ( $\rho \sim 100 \text{ mg/cm}^3$ ) and a group of 256 proportional tubes. The tubes have square cross section ( $3 \times 3 \text{ cm}^2$ ) thus ensuring a uniform thickness detection



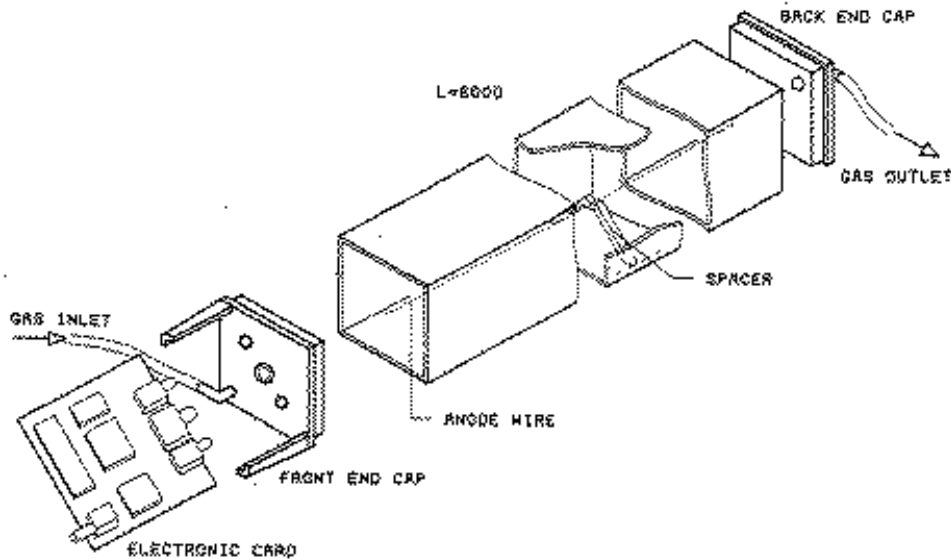


Figure 3.3: Tube layout.

layer (see Fig. 3.3).

The layers are alternatively positioned with the tube axis along the x and y directions to allow spatial reconstruction of charged tracks.

The total number of tubes inside a module is 8192.

A graphite wall of 5 cm thickness is set in front of each of the first 24 layers of the TRD acting as a 174 ton target for the  $\nu_e$ ,  $\nu_\tau$  interactions. The total length is about 3.76 m.

The last target wall is followed by eight TRD layers (as shown in Fig. 3.4), that still provide an optimal identification of the secondary particles. The total mass of the 12 basic TRD modules (including the foam and the tube materials) is about 2.4 kton. Each target wall corresponds to  $0.25 X_0$  while the entire TRD basic module corresponds to about  $7 X_0$  and  $3.5 \lambda_I$ .

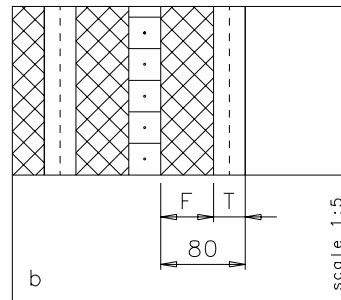
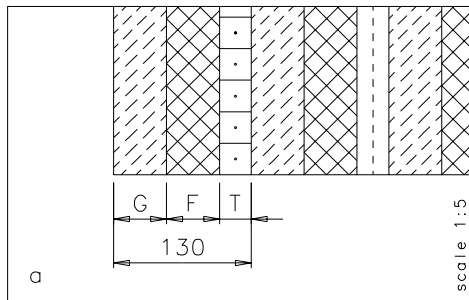
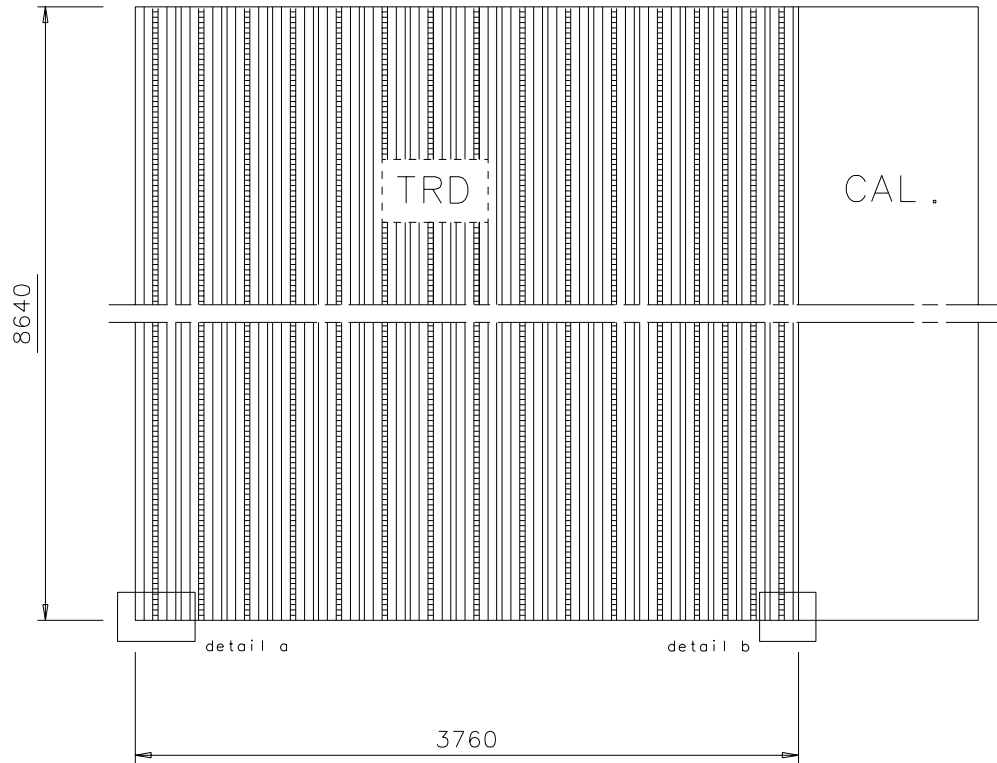
A cost saving option, in which polyethylene instead of graphite is used as target has also been considered: in this case each target would correspond to  $0.1 X_0$  while the entire module would correspond to about  $3 X_0$  and  $1.8 \lambda_I$ . The total mass would be, in this case, reduced to 1.2 kton.

In order to convert efficiently the TR photons inside a tube of  $3 \times 3 \text{ cm}^2$  cross section, we intend to try either an Ar (60%) - Xe (30%) -  $\text{CO}_2$  (10%) mixture we already tested in the MACRO TRD, or a Ar (80%) -  $\text{CO}_2$  (20%), which is less efficient, but less expensive.

In Fig. 3.5 a Monte Carlo simulation of the pion contamination versus the number of TRD layers in the above proposed setup with the two possible gas mixtures is shown. This simulation is in agreement with the MACRO TRD results [22, 23] indicated in the figure as check point.

The solution of spreading a low mass density target along the first 24 layers has been adopted for different reasons:

- the radiation length along the track of the produced electron is reduced ( $3.5 X_0$ )



G = GRAPHITE: 50 mm  
 F = FOAM: 50 mm  
 T = TUBE: 30 mm

scale 1:30

Figure 3.4: TRD layout.

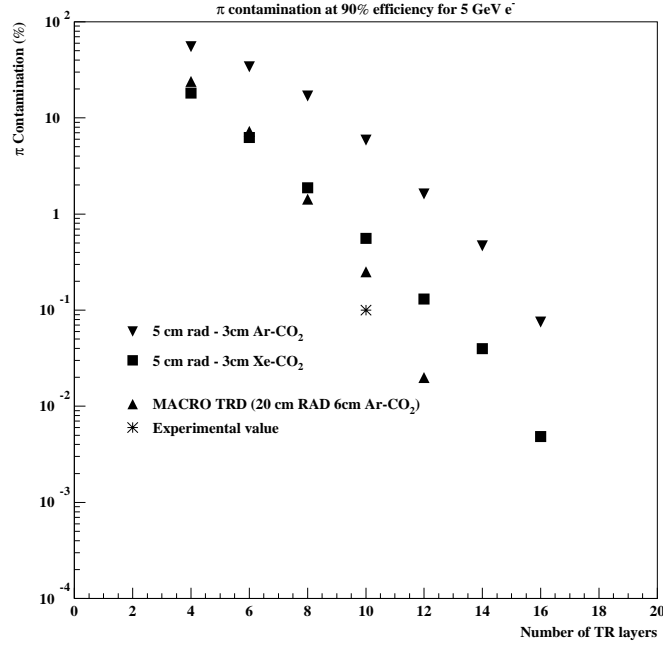


Figure 3.5: Pion contamination versus the number of crossed TRD planes (★ experimental MACRO values [22, 23])

on average), so that it can be identified in several layers without the presence of secondary tracks from the e.m. shower. Fig. 3.5 shows that the pion contamination, even with a few layers, is of the order of a few percent (about 0.1 % with ten layers).

It is also possible to give an estimate of the electron momentum in the range 0.5 ÷ 5 GeV/c using the peculiar increase of the TR yield versus the  $\gamma$  Lorentz factor as we have done in the MACRO TRD for ultrarelativistic muons (Fig. 3.6). This possibility can be interesting when the electron is produced near the detector edges and misses the calorimeter.

- with a diluted target the density of secondary tracks near the production vertex is reduced thus allowing a better multiplicity recognition and space reconstruction of the event.
- the presence of proportional tube planes, inside the low  $X_0$  target, lets a reasonable fraction of neutral pions (gammas) to travel for a few detecting layers without conversion. The lack of fired tubes near the vertex discriminates  $\pi^0$  against electron induced showers starting from the interaction vertex. Fig. 3.7 shows the fraction of  $\pi^0$  (gammas) which do not convert in TRD layers, versus the progressive layer number for graphite, polyethylene and aluminum for comparison. For example, 65% of  $\pi_0$  do not convert before the third layer in graphite.
- one interaction length along the tracks of charged pions corresponds to 8 layers. Hence it is possible to identify pions as m.i.p.'s in several TRD layers before they interact.

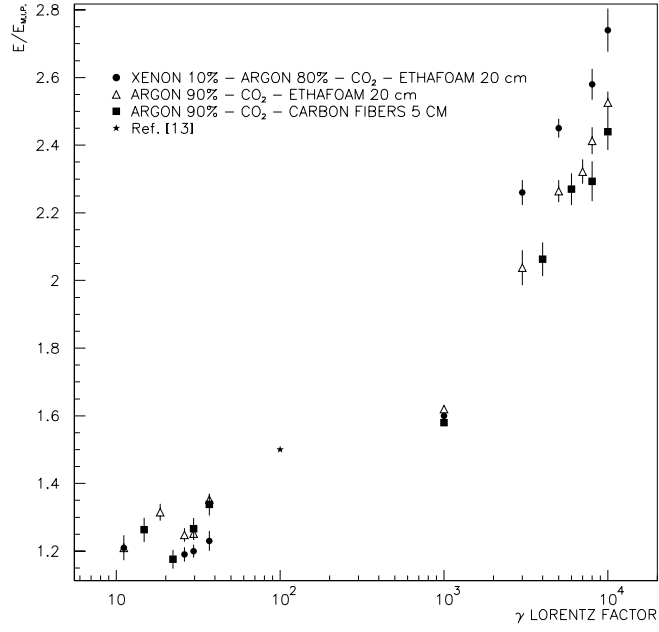


Figure 3.6: Energy deposited in TRD vs gamma Lorentz factor.

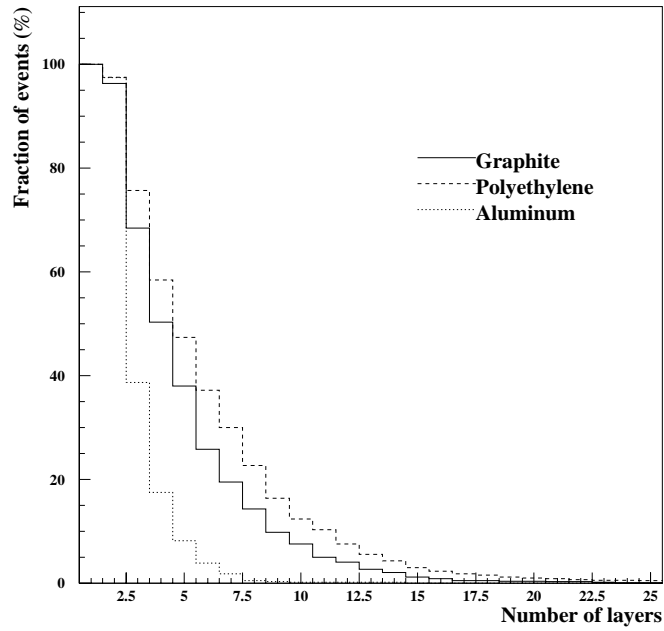


Figure 3.7: Fraction of  $\pi^0$ s that do not leave any signal in the TRD layers versus the progressive number of layers.

These considerations lead to conclude that the TRD has the ideal features for a powerful search of  $\tau$ 's decaying in electron and pion.

### 3.3.2 Proportional tube characteristics and performances

The proportional tubes used, like the MACRO TRD ones, are polystyrene extruded profiles of 0.9 mm thickness, but have a smaller cross section,  $3 \times 3$  cm<sup>2</sup>. This material is a carbon hydrogenate compound, has low density (1.1 g/cm<sup>3</sup>) and is transparent to soft X-rays of 10÷20 keV which are produced by the foam radiators when crossed by electrons above 0.5 GeV/c momentum. The tube wall absorption at the transition radiation peak (11 keV) is only 18%. In addition this material ensures good mechanical stiffness and reduced gas permeability. In fact the MACRO TRD has been mounted simply piling up tubes and radiators without intermediate mechanical frames.

The tubes are internally coated with graphite paint and grounded, while the anodic central wire is set to positive high voltage. This wire is 100  $\mu$ m thick and is positioned along the tube axis by X-shaped plastic spacers. The end-caps are equipped with gas inlet and outlet, and one of them holds the front-end electronic card, which is directly plugged to a pin soldered to the anodic wire.

The electronic channel consists of a preamplifier based on a BFR 92 high frequency transistor and a pair of cascade-connected amplifiers CLC505. With this configuration a 5.9 keV photon induced signal is formed to 20 ns F.W.H.M. [24].

## 3.4 Muon energy measurement

The TRD proportional tubes can be used to measure the muon energy in the range 1÷25 GeV/c, if this particle is identified as a clean non interacting track in any adjacent calorimeter module. This energy range nicely matches the expected muon spectrum, shown in Fig. 3.8.

As it is typically done to discriminate hadrons up to 100 GeV/c momentum using multiple dE/dx measurements in TPCs or proportional chambers, the ionization energy release inside the tubes must be carefully analysed by ADCs. In the EPI [25] detector (128 Ar gas samples each of 6 cm depth) the achieved ionization energy resolution was  $\pm 3\%$ , thus allowing to separate pions from protons at 100 GeV/c, while in the ALEPH TPC [26], the resolution was about  $\pm 4.5\%$  with 150 ÷ 300 samples, but using tracks in argon of much shorter lengths (of the order of 1.5 m).

From an inspection on the Bethe-Block dependence of the specific energy loss ( $\epsilon = dE/dx$ ) on the muon energy (Fig. 3.9), it turns out that, in order to achieve an energy resolution  $\Delta E_\mu/E_\mu$  of about  $\pm 20\%$ , the ionization energy resolution  $\Delta\epsilon/\epsilon$  measurement must be pushed to  $\pm 3\%$  in the range 1 ÷ 10 GeV/c, and to  $\pm 1\div 2\%$  in the range 10÷20 GeV/c. Therefore the instrumental stability has to be taken within  $\pm 1\%$ . In MACRO TRD this result has been obtained using a <sup>55</sup>Fe source.

Similar resolutions were achieved both by Ludlam [27] and in recent tests made at

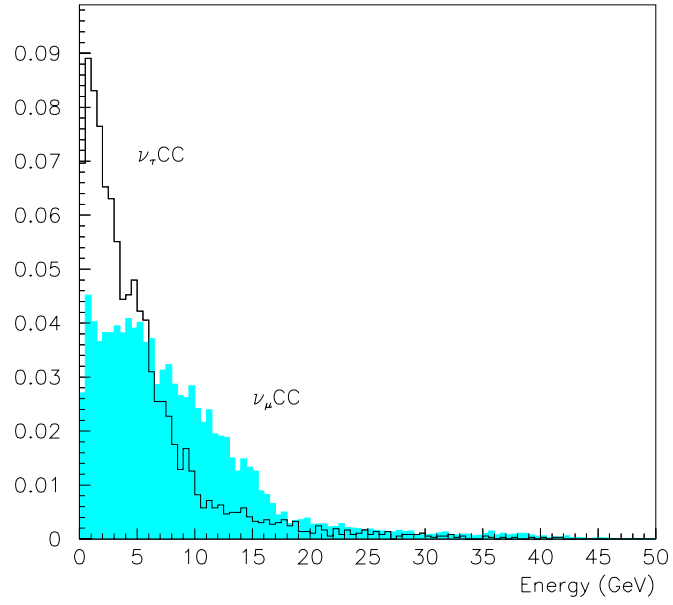


Figure 3.8: Expected muon spectrum.

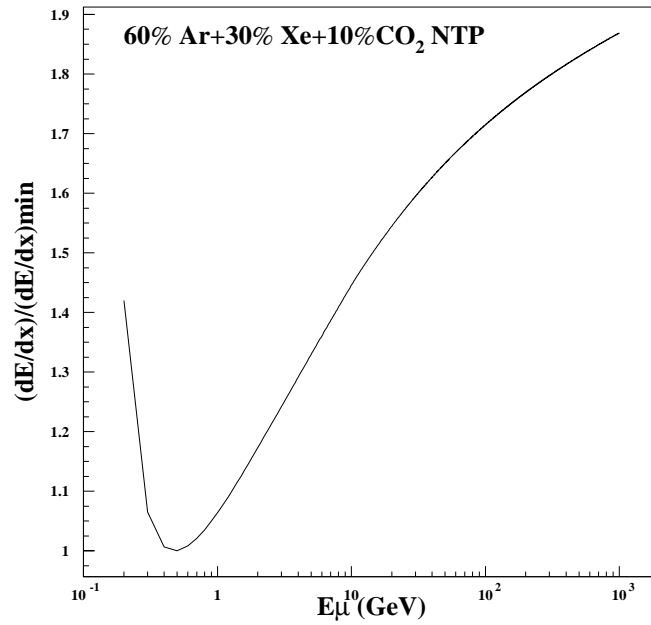


Figure 3.9:  $dE/dx$  in Argon - Xe -  $CO_2$  gas mixture.

BNL on large volume “time expansion proportional chambers“ [28, 29], where the length of the tracks crossing the gas mixture was of the order of 20÷30 cm. FADCs were used to sample the  $dE/dx$ . A frequency of at least 41 MHz was used to sample the signals (formed at about 70 ns) in time bins of 24 ns, corresponding to about 0.5 mm track length.

It has been reported [29] that 4÷5 bits are enough to analyse the energy clusters inside the time bins. A simple truncated mean procedure on the cluster pulse height should yield ionization energy resolution of about 3 % per 1 m tracks in the Argon/Xenon mixtures. With this readout, the energy of a muon track crossing more than a basic module would be measured with accuracy even better than  $\pm 20$  %, as shown in Fig. 3.10. Here these results are shown at various  $\Delta\epsilon/\epsilon$  or track length for the Ar-Xe mixture. The asymmetry of the widths of the energy resolution ( $\sigma_{LEFT} < \sigma_{RIGHT}$ ) is due to the logarithmic dependence of  $dE/dx$  on energy.

### 3.4.1 Experimental tests on proportional tubes with cosmic rays

In order to test the capability of the electronic channels to reach the ionization energy resolutions quoted above, a 1 m long proportional tube of  $3\times 3$  cm<sup>2</sup> cross section has been prepared, equipped with a card built according to the proposed electronics layout. The tube with an Ar-Carbon dioxide mixture (80%-20%) has been placed between two scintillator rods of the same size acting as a telescope for cosmic rays. The signal gated by the telescope was analysed by a digital scope Le Croy 9361 of 500 MS/sec resolution and 5000 tracks were recorded. The typical signal shape consisted of several peaks due to clusters of ionization resolved by the electronic readout; in Fig. 3.11 (upper part) a typical signal of 1  $\mu$ s width is shown. In order to reproduce the same signal sampling conditions as those of [28, 29] the signal has been analysed by a software procedure using time slots of 24 ns corresponding to the effect of a 41 MHz FADC, after cutting the noise at 20 mV level (Fig 3.11 lower part).

Thirtytwo different tracks have been grouped to simulate, as usually done by other authors [27, 28, 29], a unique track corresponding to about 1 m gas length, and a cut on the highest 50% values, which removes them from the total sample, has been applied to the time slots contents (truncated mean procedure). Fig. 3.12 shows the distributions of these mean values obtained from a group of 150 ”one-meter tracks” each one built as explained above. The FWHM of the distribution which is fitted by a gaussian is still fairly consistent with the expected resolution of  $\pm 3\%$  for one meter tracks. The discrepancy is mainly due to cosmic rays muon momentum spread.

### 3.4.2 Atmospheric neutrino tagging

The fast timing of the calorimeter allows to determine the direction of the atmospheric neutrino induced muons.

In order to tag the same class of events also in the TRD, all TRD module sides are enclosed in scintillator planes. The TRD module coverage is ensured by the adoption of scintillator strips of about 8 m length laid on the four sides without dead zones. The

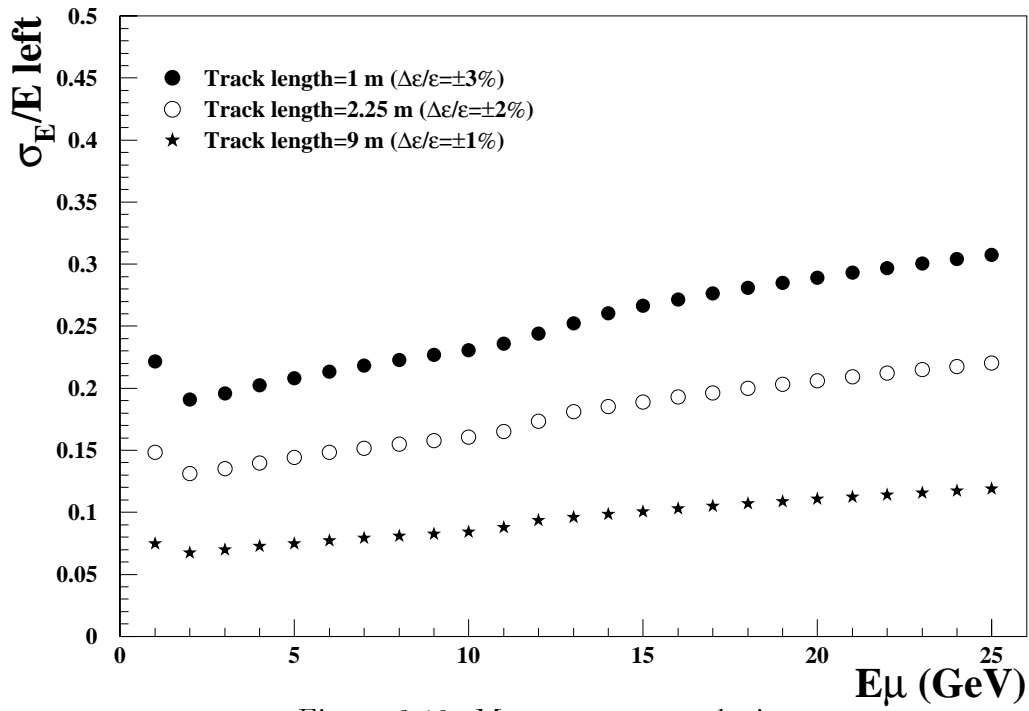
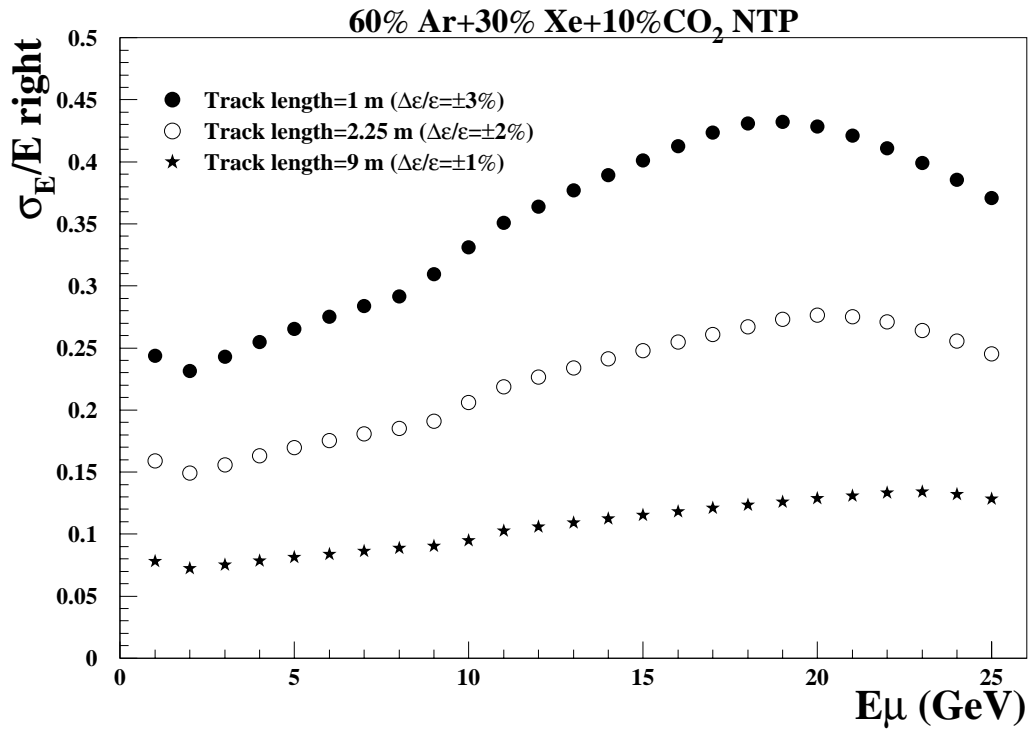


Figure 3.10: Muon energy resolutions.



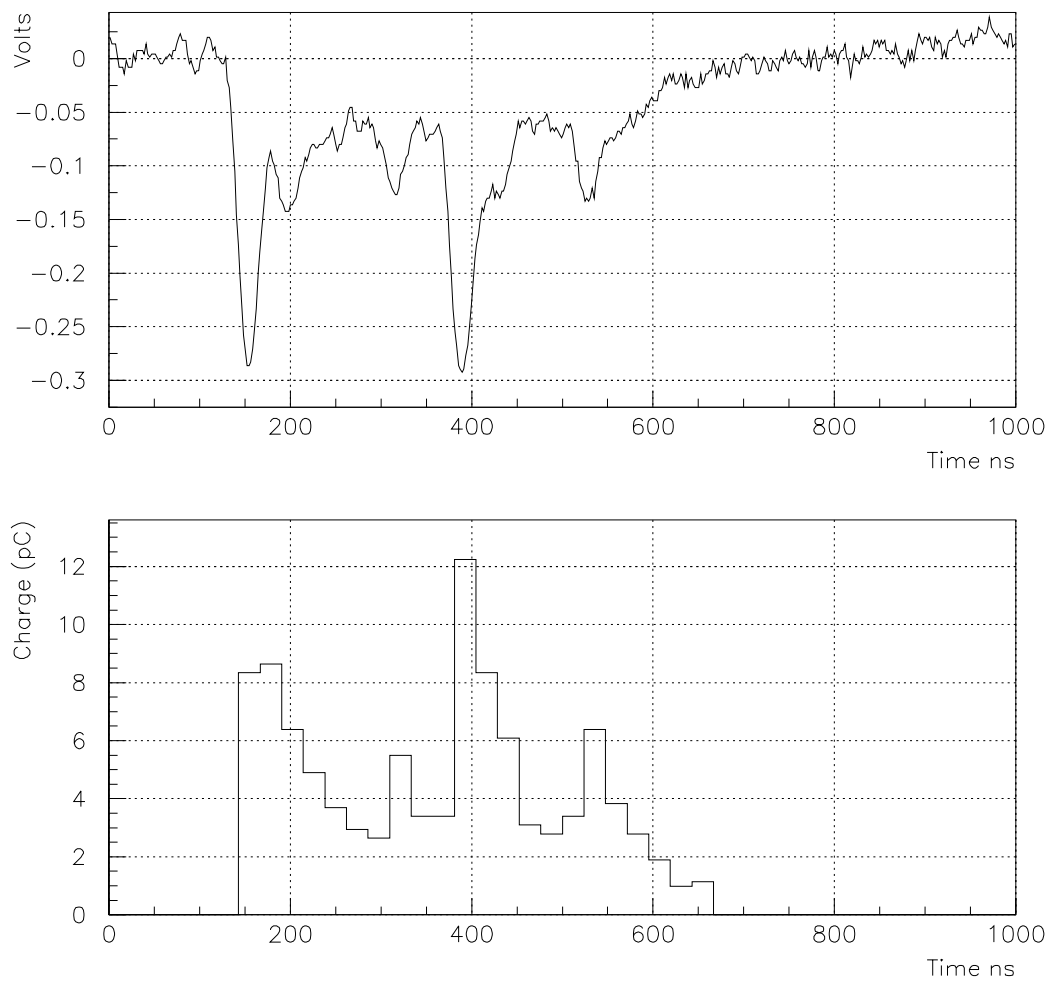


Figure 3.11: Upper part: typical signal shape. Lower part: result of the sampling procedure.

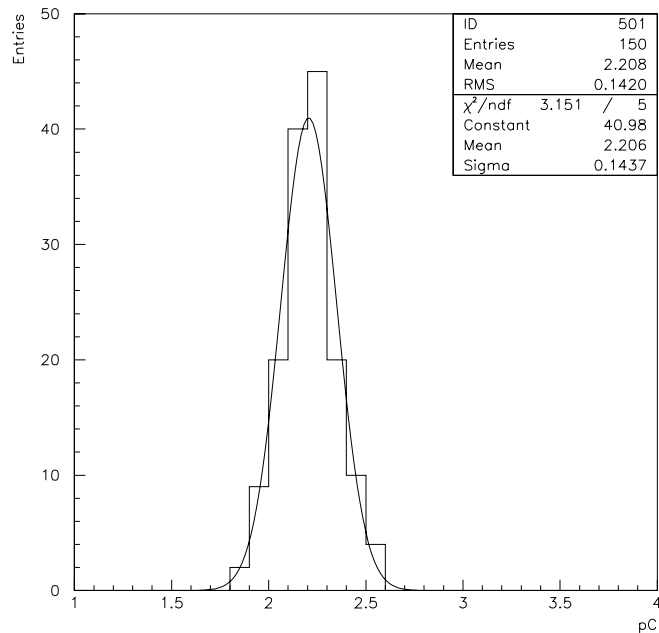


Figure 3.12: Average  $dE/dx$  for cosmic ray muons (pC).

width of the strips is foreseen to be 6 cm, while the thickness would be 1 cm. These strips would be carved for the whole length by four channels on both faces, where four WLS fibers 2 mm thick will be placed. The photons will be in this case collected independently by these two groups of 4 fibers and sent to two independent PMTs. The coincidence of the two signals will be used as marker of an external crossing muon. The strip signal can be OR-ed in groups of 32 in order to give both a trigger and a timing signal for muons impinging on the TRD. For each TRD module there would be two layers of 256 strips each. For the whole apparatus the total number of strips would be 6144.

### 3.4.3 The muon catcher

In order to measure the muon energy when the neutrino interactions occur in the last TRD and CAL targets, a muon catcher consisting of 32 layers of proportional tubes, equivalent to a TRD basic module placed at the end of the  $NOE$  detector as shown in Fig. 3.2.

In this very small fraction of events the muon energy resolution corresponds to the 1 m length curve shown in Fig. 3.10.

## 3.5 The $NOE$ calorimeter

The active part and the absorber of the calorimeter contribute to a significant fraction of the total cost of the  $NOE$  detector. Therefore different calorimeter layouts, based on the use of scintillation counters, must be carefully examined. In particular, a sampling iron calorimeter based on scintillating fibers or solid scintillator strips will be described.

Cell (cm <sup>2</sup> )	Fe (cm)	layers	$\lambda_I$	$X_0$	<i>fibers, <math>\lambda_I, X_0</math></i> (number/cell)			elec. chan.
$4 \times 4$	1.4	12x+12y	5.0	38	28	0.21	1.6	115200
$5 \times 5$	1.5	10x+10y	5.1	37	44	0.26	1.8	76800
$6 \times 6$	2.1	8x+8y	5.1	38	64	0.32	2.4	51200

Table 3.1: Main features of calorimetric bars

Features as light yield, resolutions, reliability and mechanical feasibility will contribute to the final choice.

The calorimeter design must fulfill the following requirements:

- The total mass of the calorimetric modules is  $\sim 360$  tons, in order to reach a total  $N^{\text{OE}}$  mass of  $\sim 7$  ktons.
- The sampling must be  $1 \div 1.5$  radiation length in order to achieve a good resolution.
- The module must be as short as possible in order to gain acceptance, fiducial volume and save experimental hall space.

### 3.5.1 Crossed Fiber-Bars option (C.F.B.)

A preliminary calorimeter set up has been described in the letter of intent submitted to the Gran Sasso Committee in the occasion of a call for long baseline neutrino beam proposals [16].

At that time the  $N^{\text{OE}}$  detector was composed by calorimetric bars with scintillating fibers and iron ore as active part and radiator respectively. The calorimetric technique of embedding scintillating fibers into the absorber has been developed in the past years and recently used in CHORUS [30] and KLOE [31] experiments. The calorimeter described in the following is an evolution of this technique addressed to massive detectors. In the previous letter of intent the basic calorimetric element was made by an 8 meters long bar having iron ore and scintillating fibers suitably distributed in the bar and parallel to its axis. The whole detector was made by many alternate planes of crossed calorimetric bars (Fig. 3.5.1) [18, 19].

The calorimetric bar consists of more logical cells with square cross section; the iron/iron-ore volume ratio is 0.3. In Table 3.1 the main features of the calorimeter in three different cell dimension hypotheses are shown. The numbers of total X,Y channel has been calculated assuming a two ended read out for each bar.

Fig. 3.14 shows the percentage of the active part (scintillator) crossed by a minimum ionizing particle (muon) going through the calorimeter.

At present the latest production developments of 2 mm diameter scintillating fiber leads to an attenuation length  $\lambda = 4.5$  m (Fig. 3.15) and to an increase in light yield of

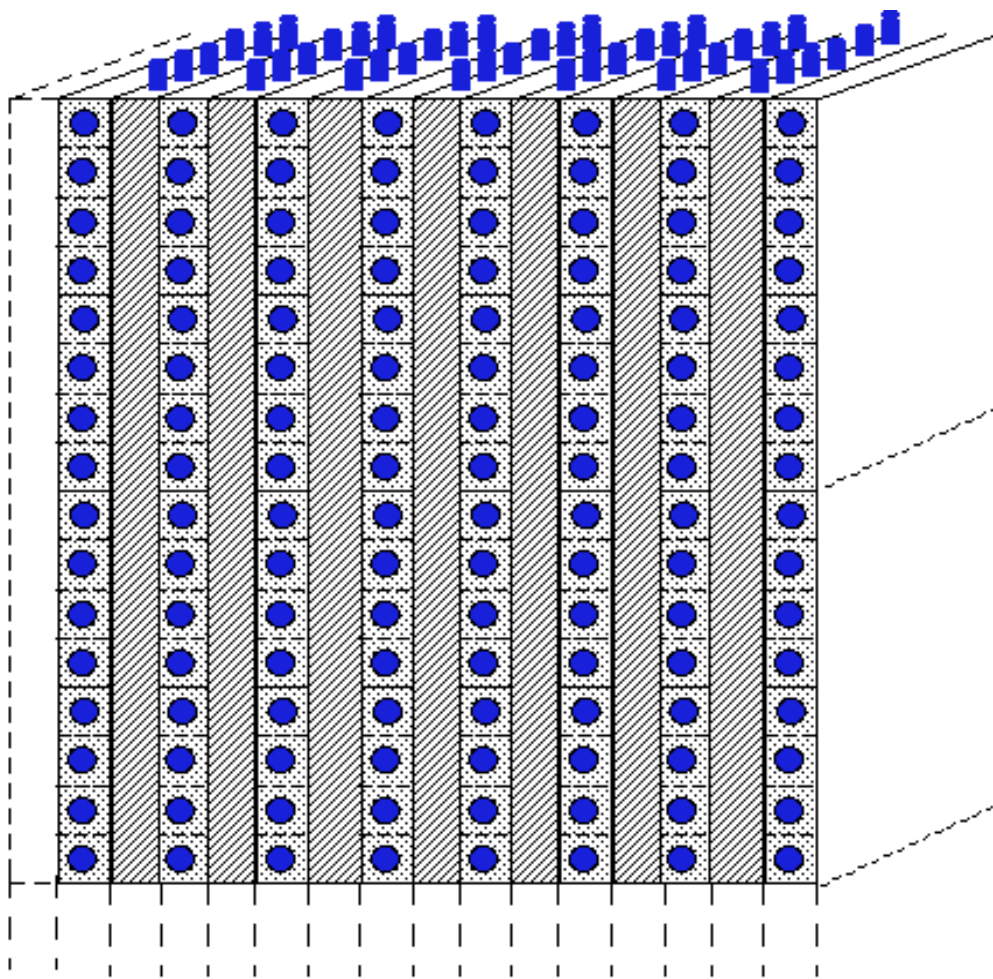


Figure 3.13: Details of the  $NOE$  calorimeter

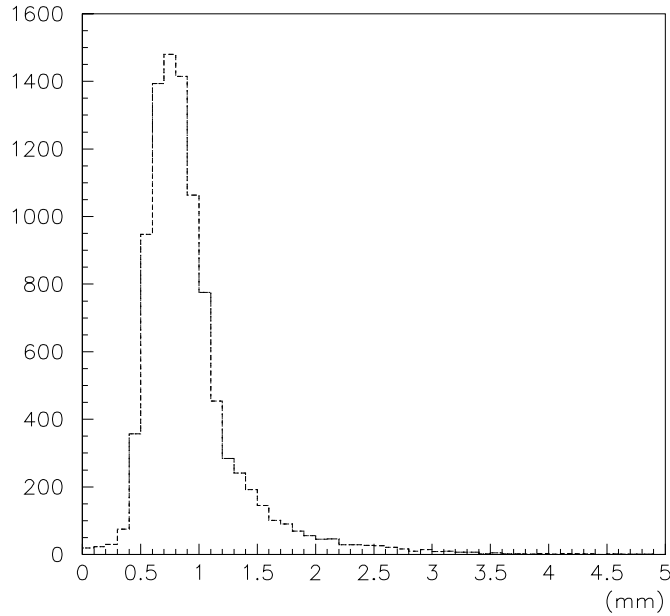


Figure 3.14: Thickness of scintillator crossed per cm of calorimeter by a minimum ionizing particle (muon)

$\%Fe$ (Weight)	$X_o$ cm	$\lambda_I$ cm	$\langle \rho \rangle$ g/cm <sup>3</sup>	$\langle Z \rangle$	$E_c$ MeV
70	5.6	44.5	3.0	15.2	37.

Table 3.2: Main features of the iron ore (hematite).

10-15 %. These figures allow to build 8 m long bars. Further investigations to improve fiber features are in progress.

In a very simple and well proven way, for each calorimetric X,Y cells, all fibers are grouped together at each side of the calorimetric bar, then sent to single or multipixel photodetector.

Concerning the absorber, the iron ore could have the following advantages:

1. it is practically cost free.
2. the radiopurity.

Fig. 3.16 shows the radioactivity spectrum of an iron ore sample. It can be inferred from the figure that iron ore acts as a screen against natural rock radioactivity and does not present any significant radioactive line above 700 keV. The very low background level leads to a low single counting rate particularly suitable to implement soft triggers for atmospheric neutrino events.

The main features of the iron ore absorber are shown in Table 3.2.

The extreme modularity of the *NOE* calorimeter allows to assemble the detector outside the gallery, greatly improving the construction efficiency.

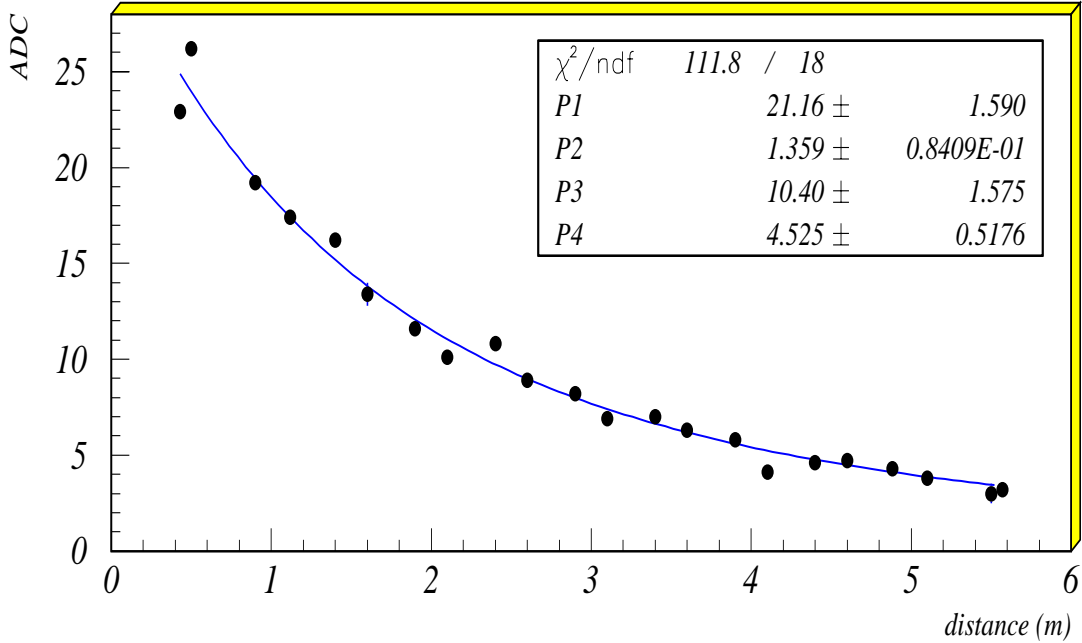


Figure 3.15: Experimental measurement of the fiber attenuation length

$\%Fe$ (Weight)	Xo cm	$\lambda_I$ cm	$\langle \rho \rangle$ g/cm <sup>3</sup>	$\langle Z \rangle$	$E_c$ MeV
72.4	5.5	45	3	21	27.4

Table 3.3: Average features of the calorimeter absorber.

It is worth noting that the intrinsic granularity of the proposed calorimeter is very high: the average distance between the fibers inside the absorber is of the order of 3 mm.

### 3.5.2 Crossed Fiber-Planes option (C.F.P.)

A detail of the detector is shown in Fig. 3.17 [20, 21]. In particular in Fig. 3.18 an 1/1 view of a calorimeter detail is shown.

Very thin iron sheets ( $\sim 2$  mm) provide the mechanical support for two planes of fibers embedded into the absorber. Fiber planes are positioned at both sides of the iron sheet, rotated  $90^\circ$  one with respect to the other. Each plane consists of self-supporting slabs made of extruded iron ore and recycled plastic. The 6.5 mm thin slab is made of two identical profiles which provide the fiber housing (Fig. 3.19).

The iron sheets are hung to a supporting mechanical structure. The general features of this calorimeter are shown in Table 3.3.

Such a layout allows a very fine sampling in the two views, which improves the accuracy of the shower axis determination. Moreover each pattern element is seen at the same time

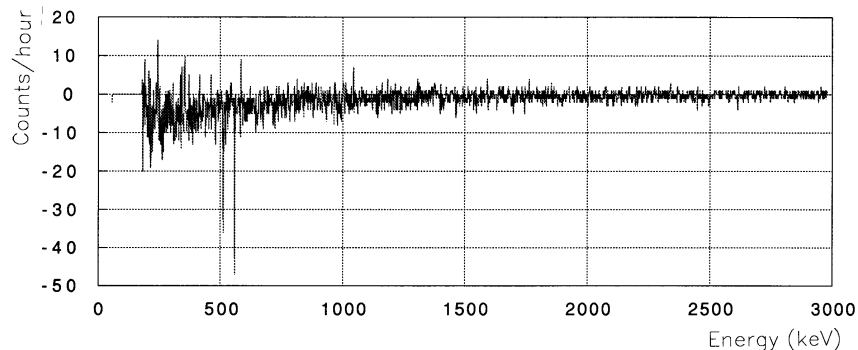


Figure 3.16: The radioactivity spectrum of an iron ore sample, after the subtraction of the environmental radioactivity.

Cell (cm <sup>2</sup> )	layers	$\lambda_I$ tot.	$X_0$ tot.	<i>fibers, <math>\lambda_I, X_0</math>/cell</i>			elec. chan.
4 × 4	60 (xy)	4.2	29	14	0.14	.97	288000
5 × 5	48 (xy)	4.3	29	22	0.18	1.2	184320
6 × 6	40 (xy)	4.2	28	32	0.21	1.4	128000

Table 3.4: Main calorimeter features in the Crossed Fiber-Planes option

in the X and Y projections. With respect to the previous option the fiber density is unchanged, therefore half of the fibers are X (and half Y) oriented, thus doubling the read out channels. Table 3.4 shows the main parameters of this calorimeter layout. The number of total XY channels has been calculated assuming two ended read out for each calorimetric cell.

The plastic and iron ore extrusion has been extensively developed and tested by two different factories that manufactured very high quality product with a density up to  $\rho = 3.6 \text{ g/cm}^3$  (see Fig. 3.20).

The additional cost of the extruded plastic and iron ore slab, only partially compensated for thinner iron sheet, is the major drawback of this solution.

### 3.5.3 Crossed Scintillator Strip option (C.S.S.)

Recently the interest towards extruded scintillator strips with wavelength shifter rods or fibers (WLS) has been rising and such devices have already been employed [34, 35, 36] (among others, also by some *NOE* collaborators).

Light produced by the passage of particles through the strip may be captured inside a WLS fiber. The fiber re-emits the light isotropically and some of that will be transmitted

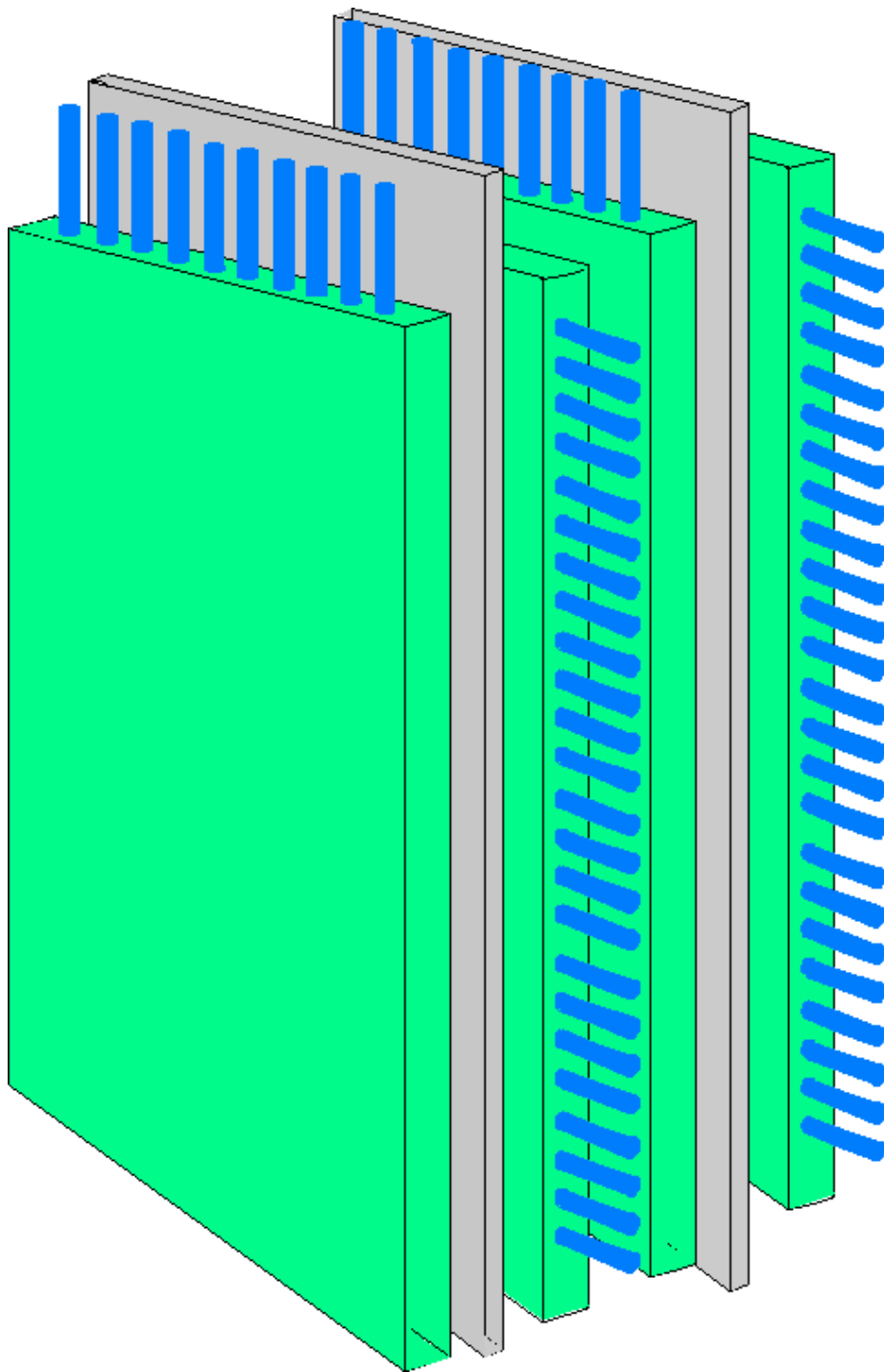


Figure 3.17:  $NOE$  calorimeter details (fibers, absorber and mechanical supports)



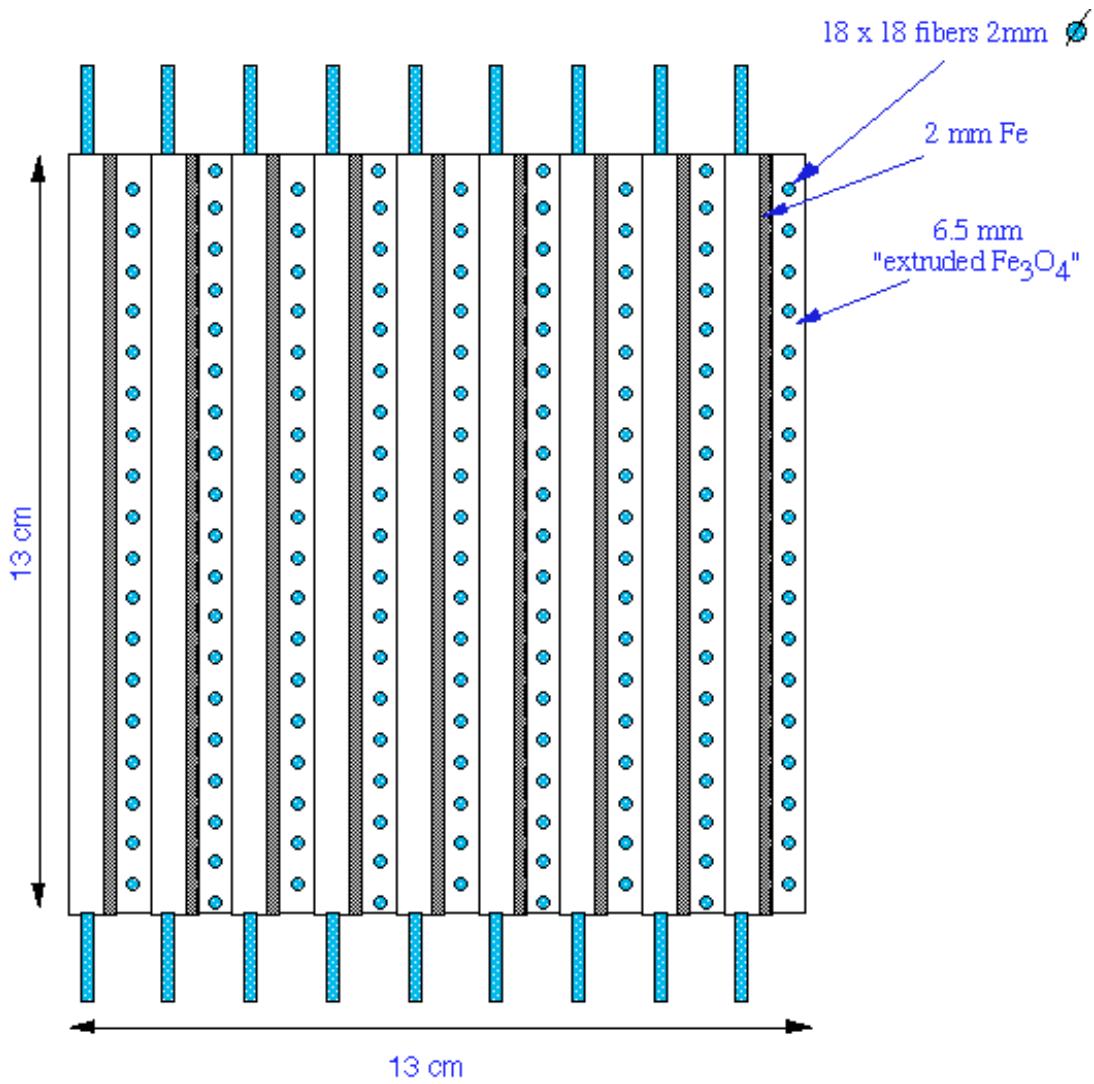


Figure 3.18:  $NOE$  calorimeter details (fibers, absorber and mechanical supports)

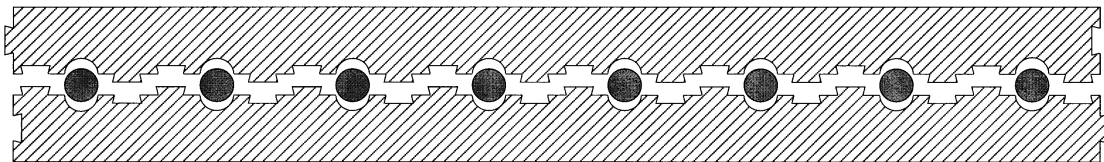


Figure 3.19: Self-supporting fiber housing

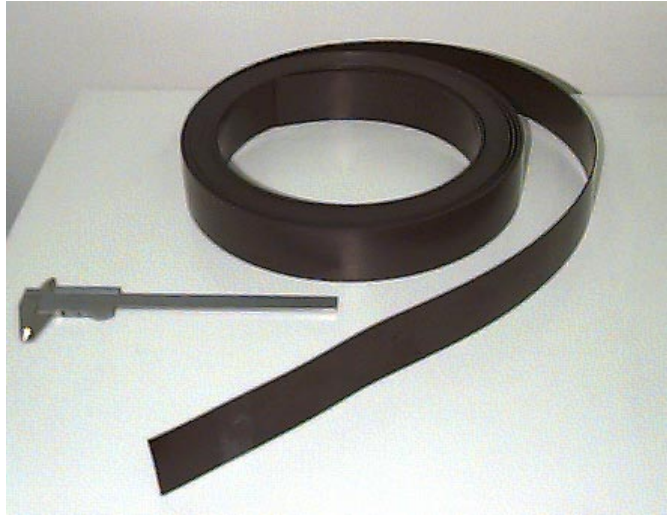


Figure 3.20: Picture of a 8 m long extruded prototype.

Cell (cm <sup>2</sup> )	Fe (cm)	layers	$\lambda_I$	$X_0$	$\lambda_I, X_0/cell$		elec. chan.
$1 \times 4$	1.5	23x+23y	4.6	41	.1	.89	220800
$1 \times 2$	1.5	23x+23y	4.6	41	.1	.89	445600

Table 3.5: Main calorimeter features in the Crossed Scintillator Strip option

out to the photodetector. The device is simple, robust and not expensive. Moreover, the extrusion reduces the manpower required for assembly. These considerations lead to the iron sampling calorimeter shown in Fig. 3.21. In the  $N^{OE}$  calorimeter all extrusion strips can be 8 m long arranged in X,Y planes faced to the iron slab absorber.

The number of total X,Y channels has been calculated assuming two ended read out for each strip. The principal disadvantage of the scintillating strips with WLS fibers is the light yield strongly suppressed by the light capture probability in the fiber. Many tests have to be done to optimize the strip dimension and the fiber diameter as well as the scintillator chemical composition in order to collect enough photoelectrons to achieve good efficiency and resolution. The main calorimeter parameters are reported in Table 3.5.

## 3.6 Photodetectors

The conservative solution of the  $N^{OE}$  calorimeter read out is based on the commercially available single PMT or 16 channel Hamamatsu R 5900 00 M16 multianode photomultiplier which has 4 mm  $\times$  4 mm pixel size.

Recently, the technology of multichannel photodetectors had a significant improvement. These devices are becoming more and more available and the  $N^{OE}$  calorimeter could

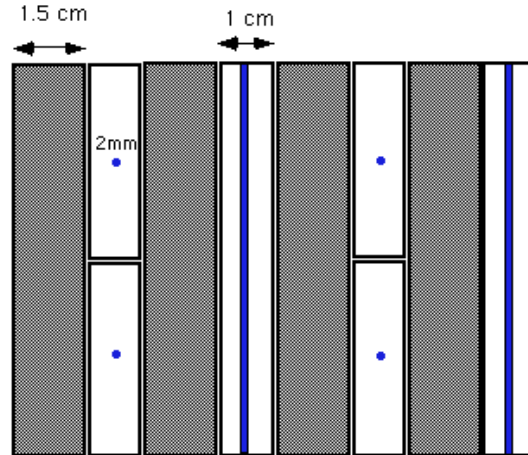


Figure 3.21: Calorimeter stratigraphy in the crossed scintillator strips option.

benefit of such a superior technology, thus improving the quality of the event pattern. Taken into account reliability, cost and power dissipation, 100k read out channels are the extreme limit in the use of single photomultipliers. For higher numbers, the use of a new high technology multipixel device at low cost is mandatory.

Two new optical devices will be examined: hybrid photodiodes (HPD) and multipixel Electron Bombarded CCD (EBCCD).

### 3.6.1 HPD's

HPD tube [32] is a fast device with very simple structure, high linearity and great reliability, made of an ordinary photocathode mounted in front of a semiconductor diode. Between them there is a vacuum gap and they are held at a voltage of few kvolts. An incoming photon is converted on the photocathode into a photoelectron, then accelerated and focussed towards a reverse biased silicon diode by an electrostatic focusing system.

Two focusing systems can be used:

- An electro-statically focused HPD, that demagnifies the spherical shaped input photocathode (e.g. 40 mm diameter) to a smaller spot anode (e.g. 11 mm), where the diode is located.
- A proximity focused HPD, with photocathode and diode of identical size active area, separated by a small gap where the electric field is planar and uniform.

In both devices the accelerated photoelectrons bombard the diode generating electron hole pairs gain, proportional to the accelerating voltage. The current can be detected and amplified by a charge amplifier.

Without power consumption, that is a fundamental feature for many channel experiments, the HPD shows high linearity (many orders of magnitude), stability (0.1%), good timing and extremely high photoelectron resolution.

Since the photocathode is imaged onto a silicon chip, by subdividing the silicon diode in pixels, HPD can become a position sensitive device very useful for  $N^{\text{OE}}$  purposes in order to reconstruct the event topology. It is worth remarking that the ability to measure as correctly as possible kinematical and geometrical parameters of the event (energy, coplanarity, direction of the shower axis, etc.) allows to improve the event reconstruction when the  $\tau$  lepton coming from  $\nu_\tau$  CC is produced in the calorimetric target.

The photoelectron pattern is imaged onto the silicon chip anode with micron accuracy. The silicon diode segmentation is not a limit, since with appropriate bias voltage very little diffusion can occur within the chip, so the HPD position resolution are limited only by the light concentration on the photocathode. Recently, 20-150 pixel tubes are available from DEP industry.

### 3.6.2 Electron Bombarded CCD (EBCCD)

This device consists of an electrostatically focused image intensifier vacuum tube with a backside bombarded thinned silicon pixel array CCD in place of the phosphor screen. Single photoelectron detection capability and inner gain (electron-hole pairs per photoelectron) tunable from 500 to 4000 are achievable. The front end electronics performs fast image read out (10 Mhz clock).

A megapixel Electron Bombarded CCD (EBCCD) has been developed by INFN and Protvino in collaboration with the russian industry Geosphaera. As in HPD device the restriction on the number of channels per EBCCD tube comes from the maximum number of fibers that can be seen by the photocathode. New samples of EBCCD tube with the same features but with a photocathode diameter of 80 mm and an image demagnification of 5 have been designed and are under test.

## 3.7 Calorimeter read out

### Crossed Fiber Bar Option

In the crossed fiber bar option (Table 3.1) the calorimeter light signals can be read by a classical, reliable and low cost photomultipliers. In  $5 \times 5$  cm<sup>2</sup> cell segmentation about 20 phe's are produced by a minimum ionizing particle. The good signal features and the number of channels to read, make the single PMT the most safe and convenient solution for this layout.

In this option, for each calorimetric X,Y cell, all the fibers can be grouped together at each side on 3/4 inch R4125 HAMAMATSU PMT's, thus collecting all the light and maximizing the electronic signal. In fact, unless the calorimeter segmentation is further pushed, the end fiber spot to photodetector pixel area ratio could be too large for a multipixel read out solution. As a consequence, the use of multipixel devices (R5900M16

HAMAMATSU PMT or HPD) needs a Winston cone light concentrator [37] to carefully match up the fiber spot to the multipixel photodetector.

### Crossed Fiber Planes Option

In the fiber planes option, the finer X,Y sampling requires more read out channels and the use of multipixel photocatode seems to be mandatory. For each channel, a Winston light concentrator is coupled to a clear fiber (1 ÷ 2 mm) or/and to a demagnifying system, such as electrostatically focusing HPD or EBCCD.

About 1800 HPD are needed to read the whole calorimeter using 100 pixels tube for  $5 \times 5\text{cm}^2$  calorimeter cell (see Table 3.4).

For the same calorimeter segmentation, assuming a working area of 80 mm photocathode diameter, 180 EBCCD tubes are required to read the whole  $NOE$  calorimeter.

In both cases, the very conservative hypothesis of a 2 mm diameter clear fiber has been considered. Using thinner fibers, the number of multipixel devices can be reduced by the square of the fiber diameter. It is worth noting that high density channels/photocathode-area largely reduces the cost per channel making possible high granularity read out. As an example, the use of 1.5 ÷ 1 instead of 2 mm fiber diameter, results in a reduction 2 ÷ 4 respectively in the number of photodetectors, thus lowering considerably the cost.

### Crossed Scintillator Strip Option

Finally, in the crossed scintillator strip option, multipixel readout like EBCCD, HPD and multi-PMT's can be easily implemented: the small WLS fiber (1 ÷ 2 mm of diameter) well matches up the pixel dimension without the need of a light concentrator or demagnifying input diameter tubes (electrostatically focusing HPD). In fact, the physical light collection process automatically determines the end detector/pixel area reduction. However, in this process, a large fraction of photoelectrons are lost, thus making the light signal a bit critical for long size detector (few photoelectrons). Shape of the strip, WLS fiber diameter and reflectivity as well, must be carefully considered in order to optimize the scintillator strip to clean fiber light collection.

Either EBCCD or even proximity focusing HPD without demagnification are the best devices for this calorimeter option. About 2200 HPD are needed to read the whole  $1 \times 4\text{cm}^2$  calorimeter cells using a 100 pixel tube, or 220 EBCCD 80 mm diameter photocathode tubes.

A 73 pixel has been adopted for the calorimeter read out of the CMS detector.

In Table 3.6 the electronic read out system and the relative cost for the different calorimeter options are summarized. In this evaluation, amplifiers, dividers, power supplies, crates, cables and connectors are included.

The HPD and EBCCD device numbers are calculated in the worst case in which 2 mm diameter clear fiber are used. Hence this number could be safely reduced by a factor 2 ÷ 4 as described above. A classical 16 multianode PMT solutions is also indicated.

Calorimeter Option	Photodetector type	Photodetector number	Channels	Estimated cost (M dollars)
CFB CAL $5 \times 5$ cm <sup>2</sup>	H.R4125 single PMT	73 k	73 k	7
	H.R5900 M16 (+ W. cone)	4750	76 k	4
	HPD electr. focus. (+ W. cone)	1500	73 k	3.5
CFP CAL $5 \times 5$ cm <sup>2</sup>	HPD electr. focus. (+ W. cone)	1800	180 k	5
	EBCCD (+ W. cone)	180	180 k	4
	H.R5900 M16 + W. cone	11 k	180 k	8
CSS CAL $4 \times 1$ cm <sup>2</sup>	HPD prox. focus.	2200	220 k	6
	EBCCD	220	220 k	5
	H.R5900 M16	14 k	220 k	9

Table 3.6: Calorimeter readout features: HPD and EBCCD use 2 mm clear fibers.

## 3.8 Calorimeter simulations

In this section the status of knowledge about the expected performances of the baseline detector implemented with 3 different calorimeter options will be described and compared. By using a GEANT 3.21 based Monte Carlo simulation program, the energy resolution for electron and hadrons has been evaluated. The detector simulation is performed considering:

1. The light produced by the passage of the particles is propagated along the fibers introducing gaussian fluctuation of about 15% around the estimated attenuation length.
2. According to the measured light yield for the minimum ionizing particle, a mean value of 20 p.e./MeV on each PMT is assumed. As far as the CSS option is concerned, an efficiency  $\epsilon=10\%$  is assumed for trapping inside the fiber the light produced in the scintillator strips. A statistical Poisson fluctuations is applied to the number of primary photo- electrons.
3. the gain of PMTs is assumed equal to  $1.5 \cdot 10^7$ , with allowed fluctuation of the order of 30%, to take into account both quantum conversion efficiency fluctuation and Poisson fluctuation in the number of secondary electrons extracted.

The electron and pion energy resolutions are shown in Fig. 3.22, 3.23 and 3.24 for crossed bar, crossed fiber and scintillator strip options respectively.

Crossed fiber bar(CFB) and crossed fiber plane(CFP) layouts have similar energy resolution behaviour, since parameters as fiber density, sampling, radiator and interaction length are practically equal.

From these first results, these kinds of scintillating fiber calorimeters seem to allow a valid energy measurement: a good energy resolution is obtained and it seems possible to obtain almost equal signals for electrons and hadrons of the same energy.

The crossed scintillator strip option (CSS) shows a simulated resolution comparable to that obtainable in the previous fiber layouts. This result is not so difficult to understand: many parameters in the described layout are very similar: the sampling frequency, the absorber material and the density.

As it will be explained in chapter 4 the tau identification is based on a kinematical selection: when tau decays, the escaping neutrino(s) will produce some missing momentum and peculiar event angular correlation as well. No missing momentum is expected in the electron and muon neutrino interactions, apart from Fermi motion and nuclear reinteraction. The most important source of "fake" missing momentum in  $\nu_\mu, \nu_e$  interactions, comes from the calorimeter performance and neutral particles escaping detection. In Fig. 3.25 the simulated transverse energy resolution for the crossed fiber planes option is shown. As a comparison in Fig. 3.26 the same resolution for the crossed scintillator strip calorimeter is reported.

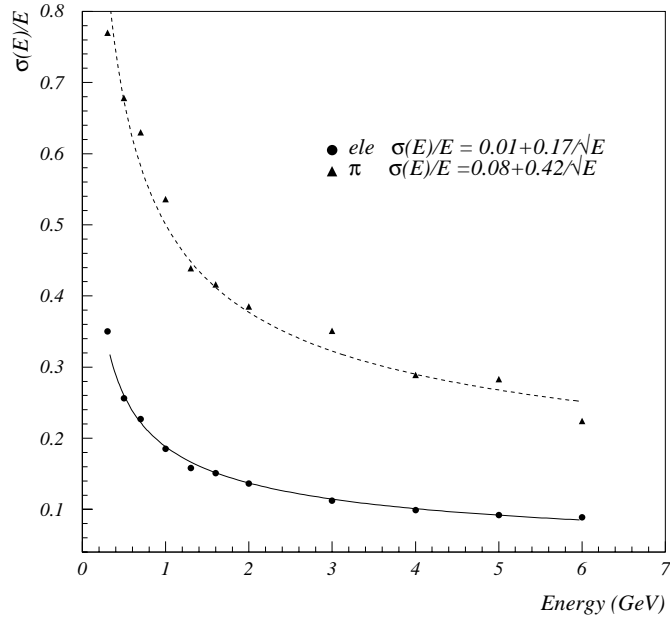


Figure 3.22: Simulated energy resolutions for electromagnetic and hadronic showers for the CFB calorimeter options.

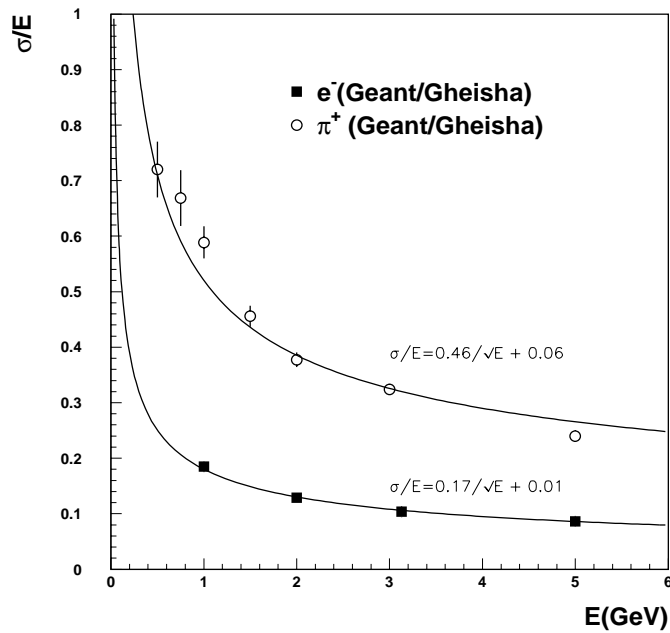


Figure 3.23: Simulated energy resolutions for electromagnetic and hadronic showers for the CFP calorimeter options.



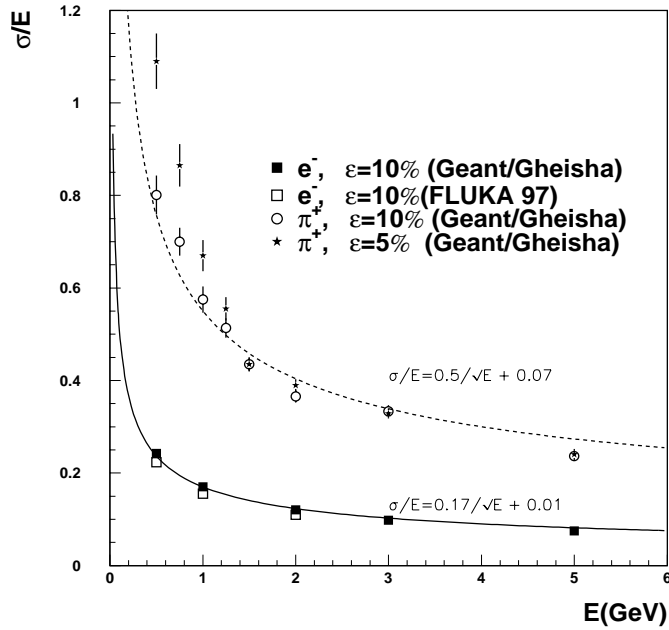


Figure 3.24: Simulated energy resolutions for electromagnetic and hadronic showers for the CSS calorimeter option.

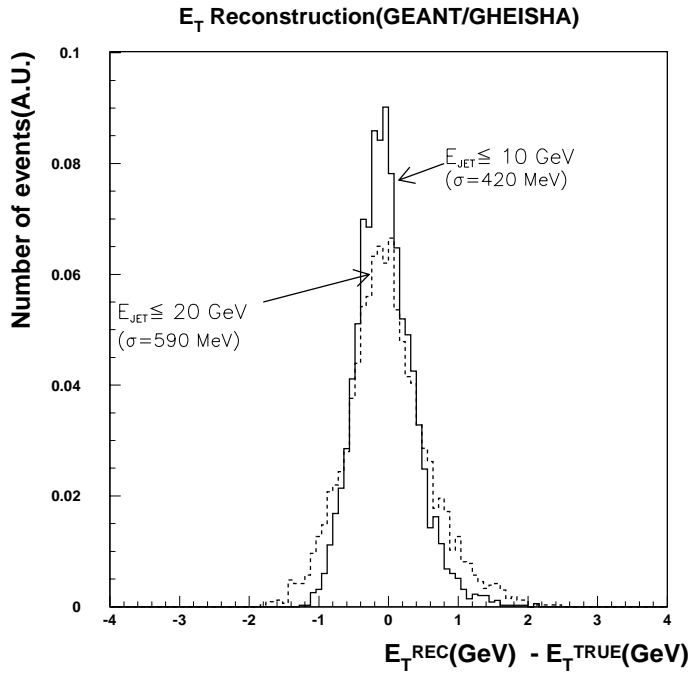


Figure 3.25: Distribution of the difference between the true and the reconstructed jet transverse energy for the CFP calorimeter option.

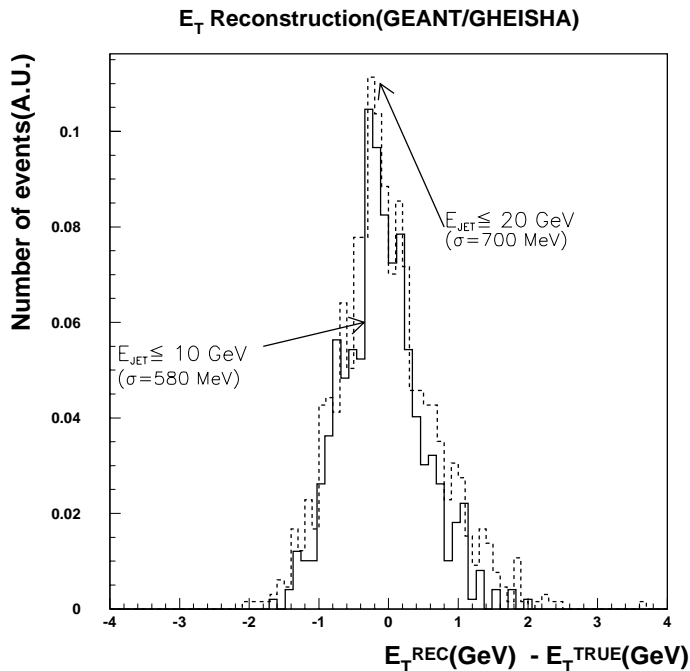


Figure 3.26: Distribution of the difference between the true and the reconstructed jet transverse energy for the CSS calorimeter option.

Although the energy resolution of the three calorimeter configurations is roughly the same, it turns out that the most expensive configuration (CFP) represents the best solution as far as the hadronic shower axis determination and the transverse missing energy reconstruction are concerned. These parameters are relevant features to improve the kinematical rejection of  $\nu_\tau$  CC against  $\nu_\mu$  CC  $\nu_e$  CC.

The decision about the best calorimeter layout will be made after accurate technical studies concerning mechanical and electronic feasibility and reliability, noise effects on the resolution, and cost. The stability of the performances (energy resolution, shower axis reconstruction, etc.) around the calorimeter equipment working conditions, (performances plateau) has to be the main goal in finalizing the experimental setup.

After a quick look, it turns out that the fiber solution allows to have enough light signal and a proven technique in a layout that has to be optimized from the mechanical point of view. On the other side the strip solution is very interesting for the ease of the construction, but it has to be carefully optimized for the poor light yield. The *NOE* R&D program continues, making rapid progresses with the goal to optimize the detection techniques.

### 3.9 Calorimeter prototype (crossed fiber bars) test

In this section, the calorimeter prototype built to study the energy resolution of the basic fiber calorimeter configuration, is described.



Figure 3.27: The calorimeter prototype at LNGS

### 3.9.1 Prototype Description

The prototype consists of 24 Calorimetric Elements (CE) 1.5 m long, assembled in 8 planes with 3 CE each, as shown in Fig. 3.27. In Fig. 3.28 a detail of the calorimetric bar end is shown as well as the collected fibers on PMT. The bars are mounted on a mechanical structure that can rotate of  $90^\circ$  around a horizontal axis in order to test the apparatus either with a beam or with cosmic rays. Layers of streamer tubes  $2 \times 0.25 \text{ m}^2$  are interleaved to CE layers to allow muon tracking.

In this prototype each CE module is made of a  $13 \times 13 \times 150 \text{ cm}^3$  aluminum box in which 330 scintillating fibers, 2 mm in diameter, are inserted. Each fiber is enclosed in a plastic tube 3.1 mm external diameter.

Fibers are grouped at each end of CE's and coupled to a HAMAMATSU R5686 PMT devoted to calorimetric applications. To evaluate the gain as a function of the supply voltage for each PMT, we use single photoelectron spectra obtained by pulsing the PMT's with a green light emitting diode for different high voltage values.

A typical measured single electron spectrum resolution is shown in Fig. 3.29.

The efficiency, as a function of the supply voltage, for muon crossing perpendicularly the CE, is shown in Fig.3.30 for several threshold values.

At operating voltages of above 2.2 kV we have full efficiency to minimum ionizing particles. The working condition was chosen at  $\sim 2.3 \text{ kV}$  supply voltage, corresponding to a PMT anodic current gain of  $1.5 \cdot 10^7$ . The thresholds are set to 30 mV.

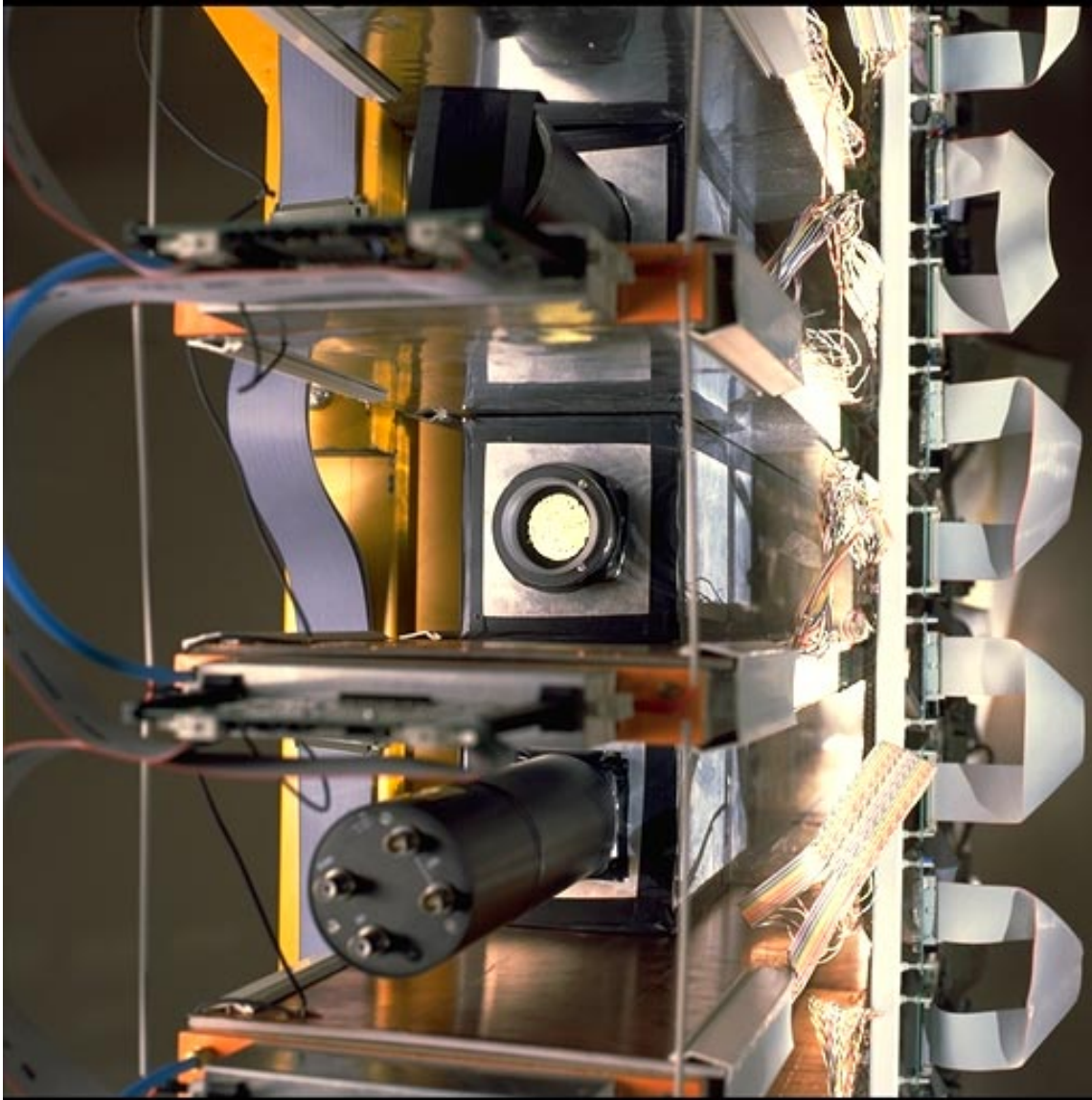


Figure 3.28: The calorimeter prototype, zoom on the lateral view.

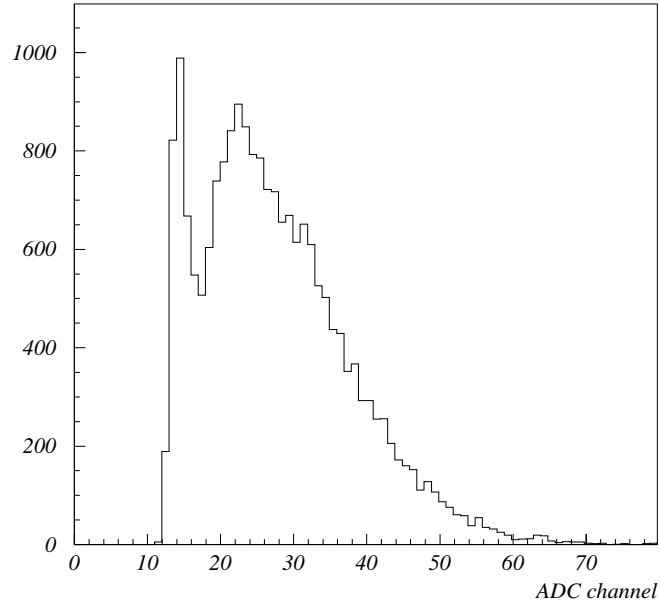


Figure 3.29: A typical single photoelectron spectrum.

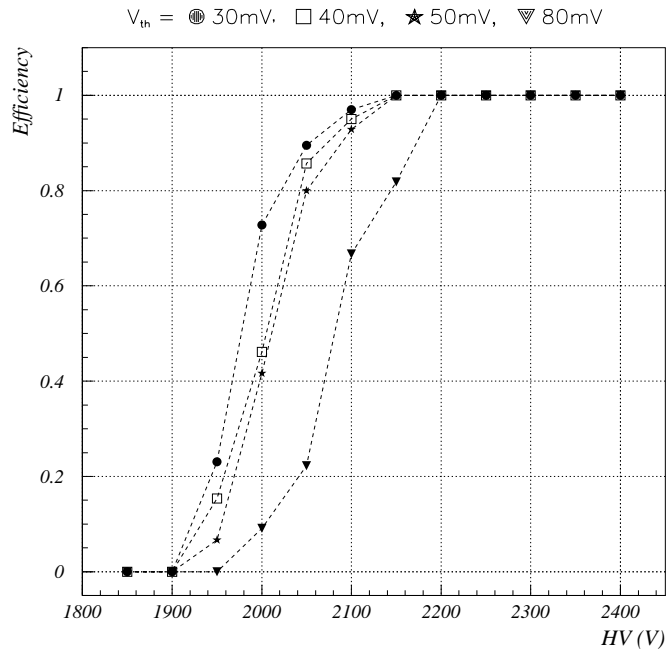


Figure 3.30: Efficiency curves of the CE crossed by cosmic ray muons for different thresholds.

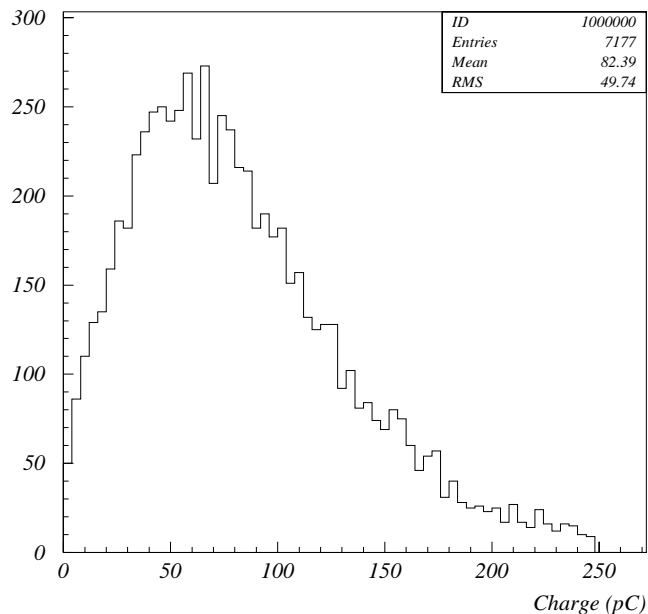


Figure 3.31: A typical charge distribution for a muon crossing a CE.

### 3.9.2 Prototype calibration with cosmic rays

The measurements described in the following are performed using only cosmic rays, with the telescope kept in the vertical position.

A tracking algorithm has been implemented to select muons and to reject showers and spurious events from the data sample. On the reduced sample of cosmic ray events, given by muons crossing the whole telescope, an analysis of the charge and time response of the prototype has been performed.

A typical charge distribution for a muon crossing a CE is presented in Fig. 3.31. The average pulse height corresponds to 30 photoelectrons at each side.

In Fig. 3.32 is shown the visible energy loss,  $dE/dx$ , for a muon crossing the telescope. This distribution, averaged over the 8 CE layers, is centered at  $dE/dx \simeq 2 \text{ MeV/cm}$  in a reasonable agreement with the total thickness of active detector crossed by a muon (Fig. 3.14). The charge resolution of 22% is comparable with that obtained dividing by  $\sqrt{8}$  the single BCE charge resolution (Fig. 3.31).

A preliminary study of the timing capabilities of this apparatus has been performed by selecting single muons crossing all the 8 CE's. Fig. 3.33 shows the time difference between the signals coming from two different CE's. To correct the time spread due to the light propagation inside the BCE the signals coming from both PMT's of a single CE are averaged. These data have not been corrected for the slewing due to the pulse height jitter.

From this measurement we estimate that a  $\sim 1 \text{ ns}$  time resolution for the 8 m long CE is achievable if the time walk due to the amplitude jitter is taken into account.

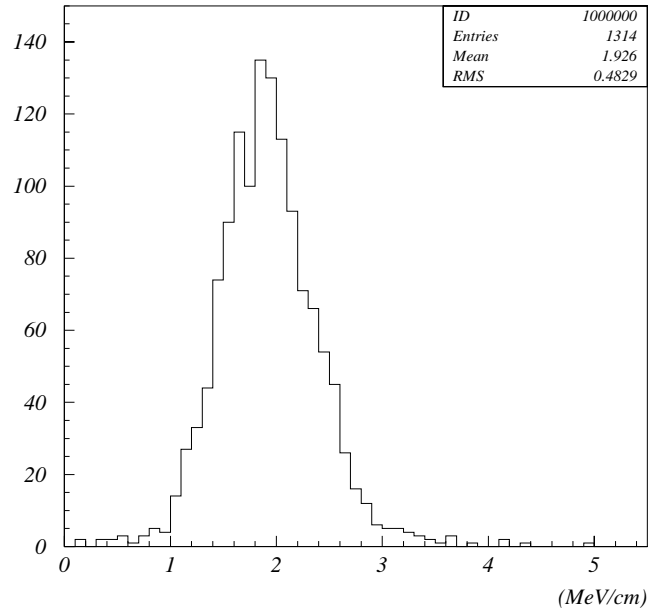


Figure 3.32: The visible energy loss of a muon crossing the telescope, averaged over the 8 CE's.

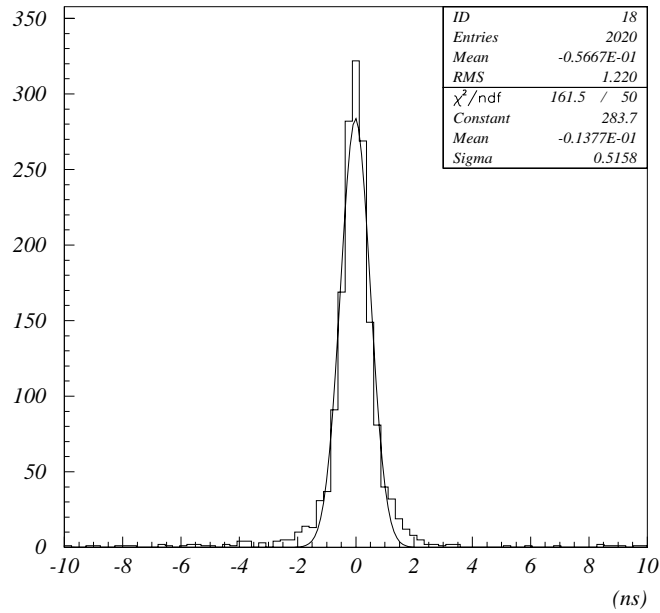


Figure 3.33: Distribution of the time difference between two CE's.

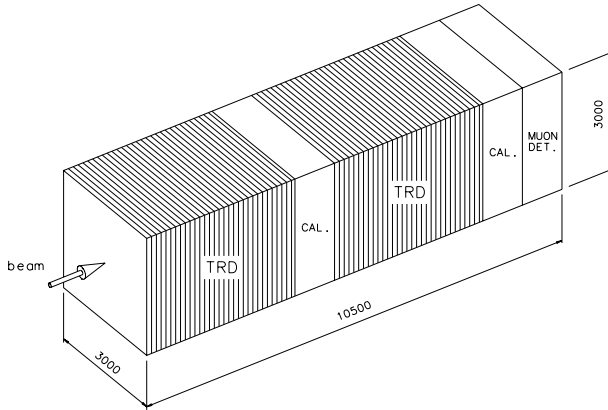


Figure 3.34: Layout of the near detector.

## 3.10 A near detector

### 3.10.1 Physical motivations

A near detector to be placed downstream the beam dump should have the primary role to compare neutrino interactions occurring in the near and far locations. In principle any significant difference at the two sites would give firm evidence of neutrino oscillations.

In particular oscillation test could be the comparison of both the energy spectra of detected interactions, the NC/CC ratios measured at the near and far locations as well as the correlation parameters as  $\phi_{l \rightarrow h}$   $\phi_{pt \rightarrow h}$  in leptonic (electron) induced  $\nu$ -events (§ 4.4). The systematic errors due to the non identical near-far  $\nu$  beam spectra require a careful study in order to justify the adoption of a near detector. In order to avoid the systematics due to possible detector differences, both detectors should be built using the same technique and should have the same granularity.

In addition the near detector gives a measure of the  $\nu_e$  beam contamination. This information is useful to evaluate the background in the electron channel oscillation appearance test.

### 3.10.2 Detector layout

The near detector will consist of some TRD modules followed by a calorimeter section and a muon catcher. In order to reduce the detector length to a reasonable size still maintaining its capability of muon energy measurement and e.m. and hadronic shower containment, we have envisaged to use two TRD-Calorimeter basic modules followed by a proportional tube muon detector, as shown in figure 3.34.



The TRD and calorimeter sections have the same depth as the far detector partners; the muon catcher consists similarly of 32 proportional tubes layers. The total length is about 10 meters, and the cross section is  $3 \times 3 \text{ m}^2$ . With this configurations we fully accept events originating axially in the first TRD, whose energy is analysed by the following calorimeter section. The muon after crossing the calorimeter is still measured by the subsequent TRD and also by the final muon detector.

Interaction originating inside the first calorimeter section are partially analysed by the second TRD and muon catcher, while the energy is conclusively measured in the second calorimeter section. Therefore the useful target is practically concentrated on the first module. The equivalent mass of the first TRD section is 23 tons, while the calorimeter section gives a contribution of about 54 tons on a total of 77 tons of useful target. The fiducial target, if we restrict the analysis on a beam transverse size of  $\pm 40 \text{ cm}$ , should be reduced to about 1 ton, namely equivalent to the targets commonly used for short base line experiments.

# Chapter 4

## Neutrino Oscillation Search

### 4.1 Introduction

Experimental results on neutrino oscillations are usually presented assuming oscillations between two neutrino flavors, as 90% confidence level excluded regions in a plot of  $\Delta m^2 = m_{\nu_i}^2 - m_{\nu_j}^2$  versus  $\sin^2 2\theta$ . In the two flavour approximation the oscillation probability may be written as

$$P = \sin^2 2\theta \sin^2 \left( 1.27 \Delta m^2 \frac{L}{E} \right) \quad (4.1)$$

where  $L$  is the distance from the neutrino source to the detector in Km,  $E$  is the neutrino energy in GeV and  $\Delta m^2$  is the mass difference in  $\text{eV}^2$ .

The apparatus can detect both atmospheric neutrinos and neutrino beam interactions. The reconstructed event direction allows an efficient separation among the two classes. Such a separation can be improved by the timing of the beam spill. Moreover, it will be possible to collect atmospheric neutrino interactions even during runs with the long baseline neutrino beam.

The time information due to scintillators and TRD will permit to distinguish the direction of incoming neutrinos and to make crucial measurements:

- the upward-travelling muon flux due to neutrino interactions in the rock **below** the apparatus will be studied looking at different event topologies (throughgoing and stopping tracks) in different energy ranges
- contained and partially contained events due to neutrino interactions **inside** the detector can be collected separating upward and downward-going particles

The good tracking resolution of the detector will allow to take into account the angular distributions. The analysis of the ratio “upward-going internal interactions / downward-going internal interactions ” will permit a strong reduction of the uncertainties connected with atmospheric neutrino flux and neutrino cross section.

In the following the sensitivity of the  $N^{OE}$  experiment in the search for long baseline neutrino oscillations will be discussed. The  $N^{OE}$  detector can perform several different

oscillation searches based on different oscillation signatures (see § 3.1). Two different kind of searches will be examined:

- $\nu_\mu \rightarrow \nu_e$  and  $\nu_\mu \rightarrow \nu_\tau$  oscillation searches based on the inclusive measurement of the muon deficit in the apparatus.
- direct  $\nu_\tau$  appearance searches based on kinematical signatures of  $\tau$  decays in  $\mu$ , electron and  $\pi$  and in two targets: TRD and Calorimeter.
- direct  $\nu_e$  appearance search, as an excess of electron events.

The measure of the ratio  $\frac{\text{no}\mu}{\mu}$  of the events without muons to the events with muons is the simpler and faster. Therefore it is mandatory for the CERN-GS LBL to plan a massive detector able to collect enough events to be competitive with other international projects (MINOS 8 kton, K2K). The 7 kton  $N^{\text{OE}}$  detector will be adequate to fulfill such a challenge. This search will be described in details in § 4.3.

The second method is more strictly an appearance search: it requires a detailed event reconstruction that can be achieved by means of a high granularity detector and will be described in § 4.4.

In the CERN  $\nu_\mu$  beam, the expected  $\nu_e$  and  $\nu_\tau$  contamination are of the order or smaller than  $10^{-2}$  and  $10^{-7}$  respectively. These figures allow to search for oscillations by looking at  $\nu_e$  and  $\nu_\tau$  appearance. In this case the detector must be able to tag the appearance of  $\nu_e$  or  $\nu_\tau$  out of the bulk of  $\nu_\mu$  events.

As shown in §3.1 the design choice of the  $N^{\text{OE}}$  detector leads to the possibility of performing independently the two searches discussed above.

With the set up described in § 3.1 a mass of  $\sim 7$  kton acting as target and detector can be considered. With this mass and the beam characteristics described in § 2.1 a total number of  $\sim 40000$   $\nu_\mu$  CC interactions can be observed in a few years.

To fix some numbers, in the following sections all the considerations will refer for reference to 40000  $\nu_\mu$  CC interactions collected on  $1.5 \cdot 10^{20}$  protons on target.

If no significant appearance signal is observed, limits to the oscillation probability of  $\nu_\mu$  can be set. This probability can then be converted into a  $\Delta m^2 - \sin^2 2\theta$  contour, at 90% confidence level, using eq. 4.1.

The experimental sensitivity is determined by the background rate, the  $\nu_\mu$  interaction rate and by the value of  $L/E$ .

## 4.2 Neutrino event generator and cross section

To optimize the  $N^{\text{OE}}$  design and to explore the detector performance in  $\nu_e$  and  $\nu_\tau$  appearance, a detailed description of the neutrino interaction features is mandatory. Moreover, the evaluation of the  $N^{\text{OE}}$  capability in  $\nu_\tau$  identification, based on kinematical criteria, requires a reliable description of the outgoing particle final state. Several codes are presently available to describe quasi elastic, resonant and deep inelastic interactions, but usually

they neglect some important effects, that should be taken into account:

**Tau polarization:**

The tau polarization affects the kinematics of the decay products, whose study is important for the  $\tau$  tagging. This effect increases the probability of background contamination from muon/electron neutrinos to the possible signal from the tau neutrino interaction followed by muonic/electronic decay of the tau.

**Nuclear rescattering and Fermi motion:**

These phenomena are important to predict the deviations of the distributions of kinematical variables with respect to the simple case of neutrino-nucleon interaction: for instance the additional production of particles might spoil the intrinsic simplicity of quasi elastic scattering producing more complicated final states (although most of additional secondary have quite a low energy) and longer tails in the distribution of transverse missing momentum.

As an example, Fig. 4.1 shows the proton momentum distribution for quasi elastic scattering of muon neutrino ( $E_{\nu_\mu}=10$  GeV) on free neutron (open circles), Carbon nucleus (black squares) and Iron nucleus (solid line) [38]. The effects of the nuclear reinteraction manifest, for instance, with the presence of extra protons of low momentum (Fig. 4.1, top) and the leading proton momentum (Fig. 4.1, bottom). The importance of these effects increases with the size of the nucleus as shown in Table 4.1. Therefore, as far as the event topology is concerned, a Carbon target gives cleaner events with respect to iron or lead.

Target	$\langle N_{n,p} \rangle$	$\langle N_{\pi^\pm} \rangle$	$\langle N_\gamma \rangle$ (MeV)	$\langle E_\gamma \rangle$	P clean event	$\langle P_\perp^{miss} \rangle$ (MeV/c)
free nucleons	1.	0	0	0	100%	0
Carbon	1.49	0.016	0.79	2.1	27.4%	175
Iron	2.26	0.023	3.42	1.5	0.	216

Table 4.1: Comparison of the result of  $\nu_\mu$  interaction ( $E_{\nu_\mu}=10$  GeV) on different targets.

For these reasons, the "light" carbon target, interleaved in the *NOE* TRD, exhibits unique features: it allows to collect quasi elastic events with good efficiency, keeping the effects of nuclear reinteractions at lower level with respect to the targets used by other planned LBL experiments.

To simulate deep inelastic, quasi elastic and resonance events, event generators that includes Fermi motion, tau polarization and nuclear rescattering inside the nucleus [38] have been used.

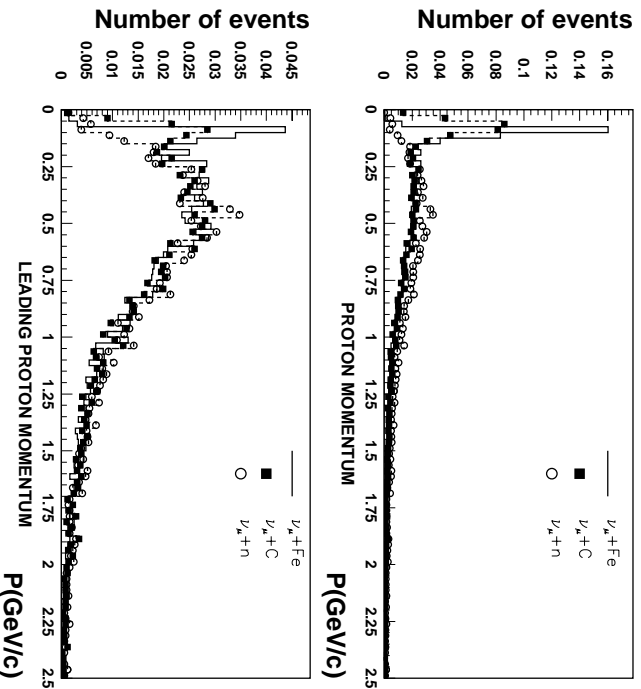


Figure 4.1: Protons (top) and leading proton(bottom) momentum distribution, in  $\nu_\mu+n$ ,  $\nu_\mu+C$  and  $\nu_\mu+Fe$  QE scattering ( $E_{\nu_\mu} = 10$  GeV)

### 4.3 Inclusive Searches

In the ideal case of a pure  $\nu_\mu$  beam and in absence of oscillations, there would be two classes of events

- $\nu_\mu$  Charged Current interactions, characterized by the presence of the muon track
- $\nu_\mu$  Neutral Current interactions, where the muon track is absent

In case of a pure beam, contributions to these classes from different neutrino flavors would signal neutrino oscillations.

In the actual case there are contributions to beam contamination (mainly electron neutrinos) that constitute the background of the experiment.

Neither Neutral nor Charged Current  $\nu_e$  interactions produce muons, so the presence of electron neutrinos in the beam, either due to beam contamination or to  $\nu_\mu \rightarrow \nu_e$  oscillations will enrich the sample of events without muons among the produced secondaries.

In case of  $\nu_\mu \rightarrow \nu_\tau$  oscillations, only a small fraction of the  $\nu_\tau$  charged current interactions produces muons: tau neutrino charged current events, where the  $\tau$  decays into hadrons or an electron, will look like neutral current  $\nu_\mu$  events in the apparatus; but in addition to the usual hadron production at the vertex, a substantial amount of hadronic energy will be added to the event from the  $\tau$  decay.

This leads to investigate appearance of  $\nu_\tau$  and  $\nu_e$  as a change in the ratio:  $\frac{N_{\mu, \text{evts}}}{N_{\nu, \text{evts}}}$  with respect to expectations. In this kind of search, based on the measure of the ratio  $\frac{N_{\mu, \text{evts}}}{N_{\nu, \text{evts}}}$ , or appearing 'NC/CC', the signatures of the  $\nu_e$  and  $\nu_\tau$  appearance are thus an increase of

appearing neutral current 'NC' and a decrease of appearing charged currents 'CC'. Such comparison has to be performed independently for the  $\nu_\mu \rightarrow \nu_e$  and  $\nu_\mu \rightarrow \nu_\tau$  channels.

However detailed event reconstruction, which could enrich the data sample recovering the low energy muons, is not essential in this inclusive method which is rather insensitive to detector granularity.

### 4.3.1 $\nu_\mu$ Event Recognition.

The identification of  $\nu_\mu$  CC events is based on the search of the long muon track in the event. The definition of this signal is achieved by imposing a cut on the penetration of the muons in the detector which implies the request of a muon energy threshold:  $E_\mu \geq 1.5$  GeV seems a cut adequate to distinguish muons from less penetrating particles.

Considering the muon energy distribution in  $\nu_\mu$  CC interactions and a conservative average energy of the  $\nu_\mu$  beam of 15 GeV, such a cut saves more than 90% of the signal.

Taking this into account, one expects a total efficiency for muon identification not smaller than 90%.

### 4.3.2 Inclusive Search of $\nu_\mu \rightarrow \nu_e$ Oscillations

In the hypothesis of  $\nu_\mu \rightarrow \nu_e$  oscillations, taking into account that in the energy range of interest the  $\nu_e$  and  $\nu_\mu$  cross sections (both charged and neutral current interactions) are approximately equal:

$$\sigma_{C\mu} \sim \sigma_{Ce} \sim \sigma_C \quad (4.2)$$

$$\sigma_{N\mu} \sim \sigma_{Ne} \sim \sigma_N \quad (4.3)$$

the  $\frac{\text{no}\mu}{\mu}$  event ratio measured in the  $NOE$  experiment can be written as

$$\frac{\text{no}\mu}{\mu} = R_{\text{obs}} = \frac{(1 - P)\sigma_N + P(\sigma_N + \sigma_C) + \varepsilon(\sigma_N + \sigma_C)}{(1 - P)\sigma_C} \quad (4.4)$$

where  $P$  is the oscillation probability and  $\varepsilon$  is the ratio of  $\nu_e$  to  $\nu_\mu$  in the beam.

The first term is due to neutral current interactions of the surviving muons at the detector, the second gives the contribution to the events without muons from neutrinos produced as  $\nu_\mu$  at the source and that oscillated to  $\nu_e$  and the latter accounts for  $\nu_e$  beam contamination.

By defining  $R_{\text{th}} = \sigma_N/\sigma_C$  we get

$$P = \frac{R_{\text{obs}} - R_{\text{th}} - \varepsilon(R_{\text{th}} + 1)}{1 + R_{\text{obs}}} \quad (4.5)$$

From this probability value and its error  $\Delta P$  obtained assuming statistical errors on  $R_{\text{obs}}$  and neglecting the error on  $R_{\text{th}}$ , the 90% excluded region contour can be drawn.

The ability to recognize the muon in the  $NOE$  detector has been discussed in the previous section. Assuming a 90% efficiency, the contour of the 90% confidence level excluded region is reported in Fig. 4.3.

It is worth noting that a 7 kton  $NOE$  detector can largely improve the  $\sin^2 2\theta$  mixing angle limit recently achieved by the CHOOZ experiment. In fact a wide region between  $10^{-1}$  and  $10^{-3}$  can be opened to the investigation.

### 4.3.3 Inclusive Search of $\nu_\mu \rightarrow \nu_\tau$ Oscillations

In the case of  $\nu_\mu \rightarrow \nu_\tau$  oscillations, using the same approximations and notation as above we have

$$\frac{\text{no}\mu}{\mu} = R_{\text{obs}} = \frac{(1-P)\sigma_N + P\sigma_N + P\eta\sigma_C(1-B) + \varepsilon(\sigma_N + \sigma_C)}{(1-P)\sigma_C + P\eta\sigma_C B} \quad (4.6)$$

where  $P$  is the oscillation probability,  $\varepsilon$  is the ratio of  $\nu_e$  to  $\nu_\mu$  in the beam,  $B$  is the branching ratio of the  $\tau$  decay in muon plus neutrinos and  $\eta$  is a kinematical suppression factor due to the  $\tau$  mass:

$$\eta = \frac{\int \Phi_\nu(E)\sigma_{\nu_\tau}(E)dE}{\int \Phi_\nu(E)\sigma_{\nu_\mu}(E)dE} \quad (4.7)$$

As above the first term is due to neutral current interactions of surviving muons at the detector, the second to neutral currents induced by neutrino tau, the third gives the hadronic contribution coming from  $\nu_\tau \rightarrow \tau$  decays, and the latter takes into account the  $\nu_e$  beam contamination.

With the same definitions as above we have

$$P = \frac{R_{\text{obs}} - R_{\text{th}} - \varepsilon(R_{\text{th}} + 1)}{R_{\text{obs}}(1 - \eta B) + \eta(1 - B)} \quad (4.8)$$

As in the previous case this formula can be used to draw the 90% confidence level excluded region reported in Fig. 4.3.

## 4.4 Direct $\nu_\tau$ appearance searches

Kinematical identification of the  $\tau$  decay, which follows the  $\nu_\tau$  CC interaction, requires excellent detector performances: good calorimetric features together with tracking and event topology reconstruction capabilities. Depending on the examined decay channel, the background is constituted of  $\nu_e$  CC events or  $\nu_\mu$  CC and  $\nu_\mu$  NC events. In order to separate  $\nu_\tau$  events from the background two basic criteria, adopted mainly by short baseline experiments, can be used:

1. an unbalanced total transverse momentum due to neutrinos produced by the  $\tau$  decay;
2. the angular correlation between  $\tau$  decay products ( $e, \mu$ ), hadronic prong and missing momentum in the transverse plane.

For  $\nu_\mu$  CC events the lepton and the hadronic shower transverse momenta are opposite and the missing momentum is not correlated with either of them.

For  $\nu_\tau$  CC events both  $\tau$  decay products and missing momenta tend to be opposite to the hadronic component. For instance in the  $\tau$  leptonic decay channels, the angle between lepton and hadrons  $\phi_{l \rightarrow h}$  is wide and similar to that between missing  $p_t$  and hadrons  $\phi_{ptm \rightarrow h}$ .

#### 4.4.1 $\nu_\tau$ appearance in the CAL and TRD ( $\tau \rightarrow \mu$ decay channel)

Simulations of  $\nu_\mu$  CC and  $\nu_\tau$  CC interactions have been performed in the total mass of the  $N^{\text{OE}}$  detector in order to reconstruct the unbalanced total transverse momentum and to obtain the angular correlation plots  $\phi_{l \rightarrow h}$  versus  $\phi_{ptm \rightarrow h}$ . Preliminary results show that it is possible to define cuts allowing to reduce the  $\nu_\mu$  CC background by a factor of  $10^2$ . Such a rejection factor and the associated  $\tau$  detection efficiency ( $\epsilon_\tau \sim 14\%$ ), are adequate to isolate the expected genuine events in the  $\Delta m^2 - \sin^2 2\theta$  region of atmospheric anomaly (see Tables 2.5 and 2.6).

Considering an exposure of  $1.5 \cdot 10^{20}$  protons on target (see § 2.1) and 40000  $\nu_\mu$  CC, a background of 129 residual  $\mu$ 's from  $\nu_\mu$  CC interactions survive after the analysis cuts. In these analyses a reduced fiducial volume, to ensure event containment and cuts on muon energy ( $E_\mu \geq 1.5$  GeV), to have clear  $\nu_\mu$  CC identification, are considered.

In absence of such a signal the sensitivity in  $\sin^2 2\theta$ , which is given by:

$$\sin^2 2\theta = \frac{2 \cdot 1.28 \cdot \sqrt{bck}}{\nu_\mu CC \cdot \eta \cdot B_{\tau \rightarrow \mu} \cdot \epsilon} \quad (4.9)$$

as shown in Fig 4.3.

#### 4.4.2 $\nu_\tau$ appearance in the TRD ( $\tau \rightarrow e$ decay channel)

The channel of tau decaying into an electron plus two neutrinos provides the best sample for  $\nu_\tau$  appearance studies due to the low background level. The  $\nu_e$  contamination in the beam gives, for  $1.5 \cdot 10^{20}$  protons on target and 14330  $\nu_\mu$  CC in the TRD target,  $\sim 140$   $\nu_e$  CC events rather uniformly distributed over the energy. Hence the required rejection is smaller than that needed for the muon channel.

As already observed, the signature of the tau production in  $N^{\text{OE}}$  will be based on kinematical analysis aiming to reject  $\nu_e$  and  $\nu_\tau$  charged current neutrino interactions. Cuts on the angular correlation between electron, hadron jet and missing momentum, allow to reduce the residual  $\nu_e$ -beam events.

The study of the  $\tau \rightarrow e$  channel needs a clear electron identification, which is strongly improved in the new detector layout, by the presence of the TRD. In fact, combining TRD and CAL information, the rejection power to separate electrons from mip particles is  $\sim 10^{-3} \div 10^{-4}$ .

The discrimination  $e/\pi$  in the TRD is based on their different behaviour in this detector: transition radiation is emitted by electrons, whereas the  $\pi$ 's (like the  $\mu$ 's) stay at the



minimum of ionization. In addition, in the TRD light material, gammas from  $\pi^0$  decays travel with low conversion probability, thus offering, in 60% of cases, the capability to distinguish neutral pions from electrons.

In the following the background sources are discussed. The residual background percentages, after the analysis cuts, are normalized to the total number of TRD  $\nu_\mu$  CC interactions, the electron efficiency is indicated as well.

- $\pi - \mu$  misidentification in  $\nu_\mu$  CC interactions with muon energy below 1.5 GeV and NC interactions with charged pions

$$\nu_\mu CC(E_\mu \leq 1.5 GeV) + NC(\pi^+ \pi^-) = 65\%$$

Taking into account the expected rejection factor ( $\sim 10^{-3} \div 10^{-4}$ ), this source of background gives no significant contribution.

- $\nu_e$  CC due to the beam contamination  $\sim 1\%$  of  $\nu_\mu$  CC,  $\sim 140$  events expected.
- $\pi^0$  coming from  $\nu_\mu$  CC interactions ( $E_\mu \leq 1.5$  GeV) and NC interactions with  $\pi^0$

$$\pi^0(\nu_\mu CC)(E_\mu \leq 1.5 GeV) + \pi^0(NC) = 32\%$$

In order to reduce the number of these background events, it will be possible to select events by requiring:

- $E_{e.m.} \geq 1.5$  GeV (most of electrons from  $\pi^0$  are below the TRD threshold, which is  $\sim 1$  GeV)

Cut	Residual $\pi^0$ bck.	Residual $\nu_e$ beam bck.	$\tau \rightarrow e\nu\nu$ efficiency
1	1.8%	90%	80%

- e.m. shower starting from the vertex ( $\pi^0$ 's appear without initial conversion in 60% of cases)

Cut	Residual $\pi^0$ bck.	Residual $\nu_e$ beam bck.	$\tau \rightarrow e\nu\nu$ efficiency
1+2	0.74%	90%	80%

- event containment

Cut	Residual $\pi^0$ bck.	Residual $\nu_e$ beam bck.	$\tau \rightarrow e\nu\nu$ efficiency
1+2+3	0.36%	45%	60%

- $\phi_{e \rightarrow h} \phi_{ptm \rightarrow h}$  correlation

Cut	Residual $\pi^0$ bck.	Residual $\nu_e$ beam bck.	$\tau \rightarrow e\nu\nu$ efficiency
1+2+3+4	0.14%	4%	30%

In absence of large mixing angle signal, taking into account the kinematical suppression due to the tau mass and the branching ratio in electron decay, the  $\sim 20$  residual background events give a sensitivity limit shown in Fig. 4.3

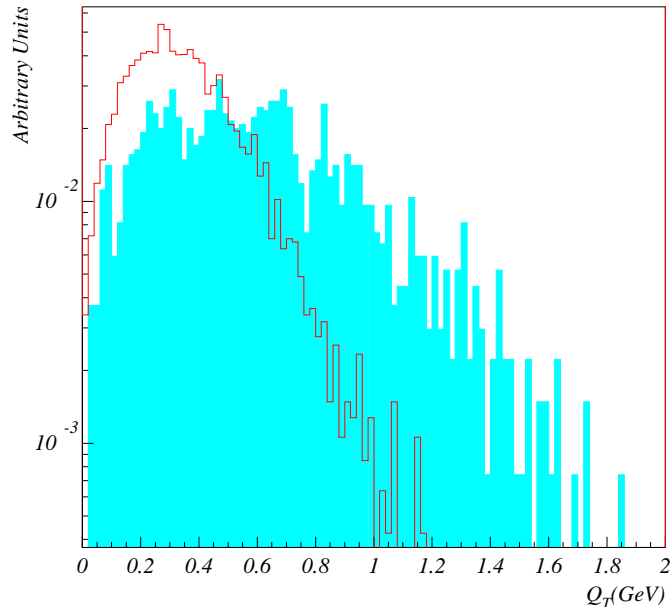


Figure 4.2:  $Q_T$  distributions for  $\nu_\mu$  NC events (solid line) and  $\nu_\tau$  CC events ( $\tau^- \rightarrow \pi^-$ ).

#### 4.4.3 $\nu_\tau$ appearance in the TRD ( $\tau \rightarrow \pi$ decay channel)

The combined use of TRD and CAL modules permits to identify the tau decay in a single hadron and a neutrino, when the interaction occurs in the TRD target. The largest background comes from  $\nu_\mu$ NC interactions; its reduction is based on kinematical cuts:

- Energy of most energetic pion  $\geq 4$  GeV.
- Missing transverse energy  $E_t < 1.5$  GeV.
- Transverse energy component with respect to the shower axis for the highest energy pion in the event ( $Q_T > 0.8$  GeV (Fig. 4.2)).

The resulting limit is shown in Fig. 4.3.

## 4.5 Direct $\nu_e$ appearance searches

### 4.5.1 $\nu_e$ appearance in the CAL target

Electrons coming from  $\nu_e$  CC can be isolated requiring the identification of hadronic and the electromagnetic shower, exploiting differences in lateral and longitudinal shower profiles.

”Electron-like” events could be produced by the decay of  $\pi^0$  generated in two kinds of background:

- $\nu_\mu$ CC interactions with muon energy below 1.5 GeV and containing  $\pi^0$ 's in the hadronic jet;

- $\nu_\mu$ NC interactions containing  $\pi^0$ 's;
- $\nu_e$ CC due to the beam contamination.

A simple cut of 1.5 GeV on the energy of the e.m. shower reduces the  $\pi^0$  contamination to 2.8% of  $\nu_\mu$  CC and 6% of  $\nu_\mu$ NC respectively.

In case of oscillations with large mixing, this contamination should not produce large effects when the signal is large enough (Table 2.5).

In absence of signal, a further cut in coplanarity can reduce the  $\pi^0$  background to a tolerable level, still keeping the electron identification efficiency at the level of 5%. All cuts applied lead to the sensitivity limit shown in Fig. 4.3.

The quasi elastic events are not enough in a LBL experiment to give a reasonable sensitivity limit. A typical q.e. event should present a simple e.m. shower in the final state. Collected q.e. events are the 5% of total signal and they are not yet completely cleaned. The background coming from NC-resonances, with only one  $\pi^0$  produced, has a cross section of the same order of magnitude of the signal. The sensitivity level in  $\sin^2 2\theta$  is of the order of  $10^{-1}$ .

#### 4.5.2 $\nu_e$ appearance in the TRD target

In the events generated in the calorimeter target, the electron is identified by using algorithms able to discriminate electromagnetic and hadronic showers, topological differences between them, minimum energy cut in e.m. shower and coplanarity as well.

It turns out that, in a dense calorimeter these strong cuts, reduce the  $\pi^0$  background and lead to an electron identification efficiency not higher than 5%. On the other side, it can be shown that the electron signature for events generated in the "light TRD" target is much more evident, as we already considered in a previous paragraph (§ 4.4.2). The main feature of this kind of event is the extremely clean electron identification by the transition radiation emitted.

In addition, in such light material 65% of  $\pi^0$  travel without conversion in the first two layers.

In the following the background sources are discussed. The residual background percentages, after the analysis cuts, are normalized to the total number of  $\nu_\mu$  CC interactions and the signal efficiency is indicated as well.

$\nu_e$  CC interactions due to the beam contamination ( $\sim 1\%$  of  $\nu_\mu$ CC  $\sim 140$  expected events) produce a background too similar to the signal, from the kinematical point of view, to allow any selection.

- $\pi - \mu$  misidentification in  $\nu_\mu$  CC interactions with muon energy below 1.5 GeV and NC interactions with charged pions

$$\nu_\mu CC(E_\mu \leq 1.5 GeV) + NC(\pi^+ \pi^-) = 65\%$$

Taking into account the expected rejection factor ( $\sim 10^{-3} \div 10^{-4}$ ), this source of background gives no significant contribution.

- $\underline{\nu_e CC}$  due to the beam contamination  $\sim 1\%$  of  $\nu_\mu CC$ ,  $\sim 140$  events expected.
- $\underline{\pi^0}$  coming from  $\nu_\mu$  CC interactions ( $E_\mu \leq 1.5$  GeV) and NC interactions with  $\pi^0$

$$\pi^0(\nu_\mu CC)(E_\mu \leq 1.5 GeV) + \pi^0(NC) = 32\%$$

In order to reduce the number of these background events, it will be possible to select events by requiring:

- $E_{e.m.} \geq 1.5$  GeV (most of electrons from  $\pi^0$  are below the TRD threshold, which is  $\sim 1$  GeV)

Cut	Residual $\pi^0$ bck.	Residual $\nu_e$ beam bck.	$e$ efficiency
1	1.8%	90%	90%

- e.m. shower starting from the vertex ( $\pi^0$ 's appear without initial conversion in 60% of cases)

Cut	Residual $\pi^0$ bck.	Residual $\nu_e$ beam bck.	$e$ efficiency
1+2	0.74%	90%	90%

- event containment

Cut	Residual $\pi^0$ bck.	Residual $\nu_e$ beam bck.	$e$ efficiency
1+2+3	0.36%	50%	50%

- Coplanarity

Cut	Residual $\pi^0$ bck.	Residual $\nu_e$ beam bck.	$e$ efficiency
1+2+3+4	0.08%	39%	39%

Considering an exposure of  $1.5 \cdot 10^{20}$  protons on target and 14330  $\nu_\mu CC$  in the TRD target, taking into account the low total background, 61 events, the sensitivity limit in the mixing angle is shown in Fig. 4.3.

Hence in the  $\nu_e$  appearance, the 7 kton LBL  $N^OE$  detector can enlarge the sensitivity limits in  $\sin^2 2\theta$  beyond the recent CHOOZ result of a factor  $\sim 25$  (see Fig. 4.3). Therefore inclusive and direct  $\nu_\mu \rightarrow \nu_e$  oscillations searches will cover a further wide region in the parameter space.

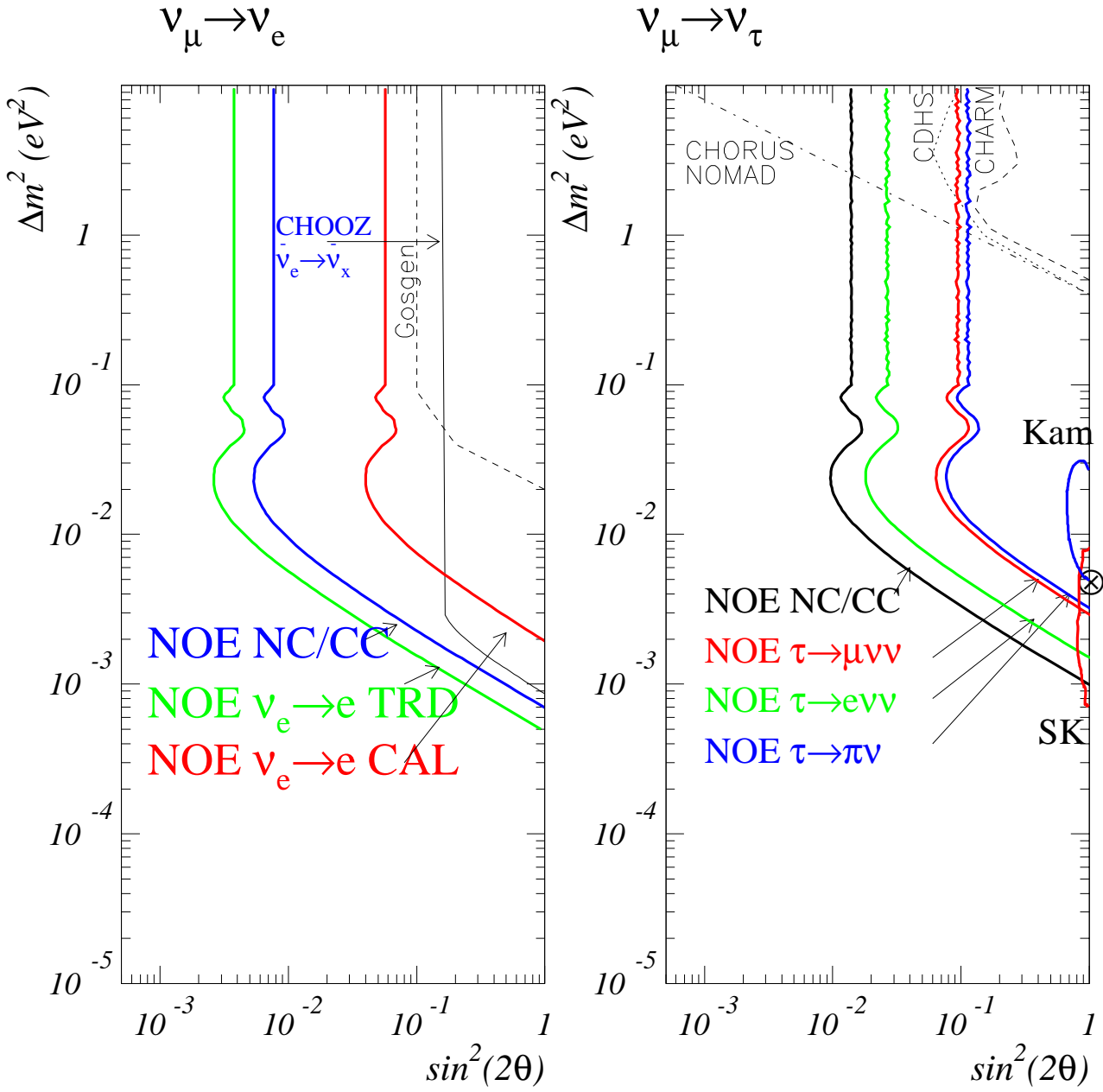


Figure 4.3: The  $NOE$  sensitivity to long baseline  $\nu$  oscillations

# Chapter 5

## Logistics, costs and time schedule

### 5.1 Logistics

The Gran Sasso Laboratories of the *Istituto Nazionale di Fisica Nucleare* (INFN) are dedicated to experiments in nuclear, subnuclear and astroparticle physics which need an efficient protection against cosmic radiation. A 10.4 km long two prongs highway tunnel goes through the Gran Sasso massif, in the central part of Italy; the Laboratories have been excavated at about 6 km from the SW entrance and 4 km from NE one. They consist of three main halls (which are conventionally named A, B and C) and of service and safety tunnels (see Fig. 5.1).

The total volume is about 180,000 m<sup>3</sup>, one half of which is devoted to the experimental activity. The floor of the experimental halls is 963 m above sea level, oriented on a geodetic (308° 50') passing through CERN. INFN has an ambitious program of excavating two new underground halls and an independent access tunnel.

The *NOE* detector is 63 m long and it can be located in hall B in the site where MACRO experiment is now in data taking up to 2000. Like MACRO, the *NOE* detector consist of 12 modules (TRD+CAL). Such a configuration allows to save the gas system and the distribution pipelines for the TRD proportional tubes. In addition the possibility to reuse part of MACRO mechanics has to be considered. In this framework other advantages are the recovery of MACRO electronic equipment as: power supply, racks and electronics. The total estimated saved cost for this recovered materials is 4 *M* dollars.

### 5.2 Cost

In Table 5.1 the breakdown of the cost is shown for the proposed detector configurations. As explained in §3.7, to be conservative, the most expensive calorimeter readout hypothesis has been considered (indicated by "double cost").

Today preliminary tests indicate that the double cost could be removed, maintaining the calorimeter read-out safe. In this hypothesis the cost reduction is 2 ÷ 3 M dollars depending on the chosen calorimeter/readout configuration.



The total cost of the  $NOE$  detector is shown in Table 5.2. The use of two subdetectors, TRD and CAL, does not add any additional cost with respect to an homogeneous detector. It has been shown that the cost per kton is indeed unchanged. In this framework the muon energy measurement is a by-product result of the TRD tasks without additional cost.

Although the energy resolution of the three calorimeter configurations is roughly the same, it turns out that the most expensive configuration gives the best resolution on the hadronic shower axis determination, thus giving a better transverse missing energy reconstruction.

### 5.3 Time schedule

The collaboration continues to carry out tests on the reference  $NOE$  detector and in particular on the calorimeter options to define the final layout. The 1998 will be devoted to build a prototype 1:1 in thickness of the basic module TRD+CAL. Several results concerning the  $e$ ,  $\pi$  discrimination, energy resolution, muon energy measurement and so on, will be obtained using this test module. Within the year 1999 results and final project must be ready. From that time about 3 years of construction are needed to complete the detector. The extreme modularity of  $NOE$  permits to implement several equipments on a parallel line. Keeping in mind the MACRO detector experience, the first modules can be operating around 2001, thus making easy to build the residual modules and to speed up the whole construction.



	Cost (M dollars)
<b>TRD</b>	
Proportional Tubes	3.5
Absorber (Graphyte)	3.8
Radiator (Foam)	0.1
Readout and ADCs	1.5
HV	0.2
Gas system	0.6
<b>Total TRD</b>	<b>9.7</b>
TRD cost/kton	4.0
<b>Calorimeter (CFB)</b>	
Fibers	7.5
Absorber (bars and Iron ore)	2
Photodetector system	4 (double cost)
Readout and ADCs	1
<b>Total</b>	<b>14.5</b>
CFB calorimeter cost/kton	3.4
<b>Calorimeter (CFP)</b>	
Fibers	7.5
Absorber (Extrusions and Iron)	5.5
Photodetector system	5 (double cost)
Readout and ADCs	2
<b>Total</b>	<b>20</b>
CFP calorimeter cost/kton	4.6
<b>Calorimeter (CSS)</b>	
Scintillator strips	2.5
Absorber (Iron)	2.5
Photodetector system	6 (double cost)
Readout and ADCs	2.5
<b>Total</b>	<b>13.5</b>
CSS calorimeter cost/kton	3.1
Mechanichs	2
Trigger, ACQ	2
<b>Total</b>	<b>4</b>

Table 5.1: Details of detector cost

Detector config.	Total cost (M dollars)	Total cost with MACRO recovery (-4) (M dollars)
TRD + CFB	28.2	24.2
TRD + CFP	33.7	29.2
TRD + CSS	27.2	23.2

Table 5.2: Detector cost (M dollars) for the three calorimeter configurations

# Chapter 6

## Conclusions

In this document the status of the  $N^{\mathcal{O}E}$  project has been discussed. This is the result of efforts done in the last year by the present Collaboration for the design of a long baseline neutrino oscillation experiment on a neutrino beam from CERN to Gran Sasso Labs.

The  $N^{\mathcal{O}E}$  design is strongly improved in the new version here presented. The new layout still have an extreme modularity as before; the Basic Module is repeated several times (12) to implement the whole apparatus. The main features of  $N^{\mathcal{O}E}$  detector can be summarized as it follows:

- It is a 7 kton full target detector.
- Inclusive measurement NC/CC gives an unambiguous test to investigate the existence of a neutrino oscillation competing with US and Japanese experimental LBL programs. A second experiment at Gran Sasso, besides the more granular ICARUS detector, must be therefore a massive detector.
- Light TRD and dense CAL detector/target can be addressed to independent class of events recovering quasi-elastic and resonant events.
- The combination of the information coming from TRD and CAL strongly improve the electron and pion identification, thus opening, besides  $\tau \rightarrow \mu\nu\nu$ , the study of other  $\tau$  decays for example in e, or  $\pi$ .
- In  $\nu_\mu \rightarrow \nu_e$  channel,  $N^{\mathcal{O}E}$  will improve the recent limit of the CHOOZ experiment of about a factor 25.
- Concerning the atmospheric neutrino studies the  $N^{\mathcal{O}E}$  experiment could be a complementary approach to the Superkamiokande water Čerenkov detector. Its fast trigger and low energy threshold ( $E_{th} \sim 400 \div 500$  MeV) should allow to measure atmospheric neutrinos down to  $\Delta m^2 = 10^{-3} \div 10^{-4}$  eV<sup>2</sup>.
- $N^{\mathcal{O}E}$  is a fine grain detector. The solutions proposed for the read-out should guarantee a good event topology reconstruction, making possible the recognition of the

events. Therefore  $N^{OE}$  is a conventional detector, which use proven techniques, with sophisticated read-out.

- $N^{OE}$  detector can be placed in Hall B of Gran Sasso Laboratories in the same location of Macro detector. The same modularity (12 modules) allows to save existing equipment as: gas system and distribution pipelines for proportional tubes, part of mechanical structure and power supplies, racks and electronics. This value has been quantified.
- The materials used in  $N^{OE}$  detector do not require particular safety conditions.
- Programs for the next future foresee a test of a TRD+CAL module prototype, at a scale factor 1:1, already approved and founded by INFN, planned for 1998-1999.

### Acknowledgements

The  $N^{OE}$  Collaboration would like to thank the whole INFN-Naples, INFN-Bari, INFN-Lecce and INFN-LNGS mechanical and electronics staff for the constant support. Special thanks are also due to M. Borriello, A. Leone and R. Rocco for their technical expertise. We gratefully acknowledge the work of A. Boiano and A. Candela in the design of the read-out electronics. We are grateful to G. Battistoni and A. Ferrari for helpful discussion on calorimetry simulation. We express our appreciation to the INFN Scientific Committee II, for the constant support and prototypes funding.

# Contents

<b>1</b>	<b>Physical motivations</b>	<b>4</b>
1.1	Introduction . . . . .	4
1.2	Hints from atmospheric neutrinos . . . . .	5
1.3	Three-Flavor Mixing . . . . .	6
<b>2</b>	<b>The CERN - Gran Sasso LBL project</b>	<b>8</b>
2.1	The neutrino beam . . . . .	8
2.2	Oscillation signatures . . . . .	10
2.2.1	Oscillating event rates . . . . .	10
2.2.2	$\nu_\mu$ disappearance . . . . .	13
2.2.3	$\nu_\tau$ and $\nu_e$ appearance . . . . .	13
<b>3</b>	<b>Experimental setup</b>	<b>19</b>
3.1	Detector design . . . . .	19
3.2	The <i>NOE</i> Detector . . . . .	20
3.3	The <i>NOE</i> TRD . . . . .	22
3.3.1	General description . . . . .	22
3.3.2	Proportional tube characteristics and performances . . . . .	27
3.4	Muon energy measurement . . . . .	27
3.4.1	Experimental tests on proportional tubes with cosmic rays . . . . .	29
3.4.2	Atmospheric neutrino tagging . . . . .	29
3.4.3	The muon catcher . . . . .	32
3.5	The <i>NOE</i> calorimeter . . . . .	32
3.5.1	Crossed Fiber-Bars option (C.F.B.) . . . . .	33
3.5.2	Crossed Fiber-Planes option (C.F.P.) . . . . .	36
3.5.3	Crossed Scintillator Strip option (C.S.S.) . . . . .	37
3.6	Photodetectors . . . . .	40
3.6.1	HPD's . . . . .	41
3.6.2	Electron Bombarded CCD (EBCCD) . . . . .	42
3.7	Calorimeter read out . . . . .	42
3.8	Calorimeter simulations . . . . .	45
3.9	Calorimeter prototype (crossed fiber bars) test . . . . .	48
3.9.1	Prototype Description . . . . .	49

3.9.2	Prototype calibration with cosmic rays . . . . .	52
3.10	A near detector . . . . .	54
3.10.1	Physical motivations . . . . .	54
3.10.2	Detector layout . . . . .	54
<b>4</b>	<b>Neutrino Oscillation Search</b>	<b>56</b>
4.1	Introduction . . . . .	56
4.2	Neutrino event generator and cross section . . . . .	57
4.3	Inclusive Searches . . . . .	59
4.3.1	$\nu_\mu$ Event Recognition. . . . .	60
4.3.2	Inclusive Search of $\nu_\mu \rightarrow \nu_e$ Oscillations . . . . .	60
4.3.3	Inclusive Search of $\nu_\mu \rightarrow \nu_\tau$ Oscillations . . . . .	61
4.4	Direct $\nu_\tau$ appearance searches . . . . .	61
4.4.1	$\nu_\tau$ appearance in the CAL and TRD ( $\tau \rightarrow \mu$ decay channel) . . . . .	62
4.4.2	$\nu_\tau$ appearance in the TRD ( $\tau \rightarrow e$ decay channel) . . . . .	62
4.4.3	$\nu_\tau$ appearance in the TRD ( $\tau \rightarrow \pi$ decay channel) . . . . .	64
4.5	Direct $\nu_e$ appearance searches . . . . .	64
4.5.1	$\nu_e$ appearance in the CAL target . . . . .	64
4.5.2	$\nu_e$ appearance in the TRD target . . . . .	65
<b>5</b>	<b>Logistics, costs and time schedule</b>	<b>68</b>
5.1	Logistics . . . . .	68
5.2	Cost . . . . .	68
5.3	Time schedule . . . . .	70
<b>6</b>	<b>Conclusions</b>	<b>73</b>

# Bibliography

- [1] K.S. Hirata et al. (Kamiokande II Collaboration), Phys. Lett. B 280 (1992) 146
- [2] R. Becker-Szendy et al. (IMB Collaboration), Phys. Rev. D 46 (1992) 3720
- [3] W.A.Mann et al. (Soudan 2 Collaboration), Phys. Lett. B 291 (1992) 200
- [4] Ch. Berger et al. (Frejus Collaboration), Phys. Lett. B 245 (1990) 305
- [5] M. Aglietta et al. (NUSEX Collaboration), Europhys. Lett. 8 (1989) 611
- [6] Y. Suzuki (SuperKamiokande collaboration), Proceedings of the 25th International Cosmic Ray Conference (Durban), (1997)
- [7] E. Kearns (SuperKamiokande collaboration), presented at TAUP97 (Gran Sasso Laboratories) (1997)
- [8] P. Bernardini (MACRO Collaboration), Proceedings of 25th International Cosmic Ray Conference (Durban), 7 (1997) 41
- [9] P.F. Harrison, D.H. Perkins and W.G. Scott, Phys. Lett. B 349 (1995) 137
- [10] Chooz Collaboration, HEP-EX/9711002
- [11] E. Weisse "Study of a CERN Neutrino Beam to Gran Sasso Laboratory", presented at Gran Sasso Meeting on Long Baseline Neutrino Experiments (November 9, 1995)
- [12] A.E. Ball, S. Katsanevas and N. Vassilopoulos, CERN/ECP 95-13
- [13] F. Pietropaolo "Long Base Line Neutrino Oscillations with Icarus", presented at Gran Sasso Meeting on Long Baseline Neutrino Experiments (December 15, 1994)
- [14] F. Cavanna "The CERN-Gran Sasso Long-Baseline Neutrino-Beam Project", CERN/PPE 95-133
- [15] V. Palladino, Proceedings of the "Fermilab Main Injector Workshop", (Fermilab) May 1997
- [16] G. Barbarino et al., " $NOE$  Atmospheric and long baseline Neutrino Oscillation Experiment", INFN/AE-96/11 (1996)

- [17] G. Barbarino et al., " *NOE* : Atmospheric and long baseline Neutrino Oscillation Experiment", Nucl. Phys. B 48 (1996) 204-206.
- [18] G. Osteria et al., proceedings of the " 7th Pisa meeting on advanced detector", Isola d' Elba, Italy, May 25-31, 1997.
- [19] G. Barbarino et al., " *NOE* : A Scintillating Fiber Calorimeter to Search for Long Baseline Neutrino Oscillations", Proceedings of the 25th International Cosmic Ray Conference (Durban), (1997) vol.7 p.101
- [20] G. Barbarino et al., "The *NOE* detector for a long baseline neutrino oscillation experiment", presented at TAUP97 (Gran Sasso Laboratories) (1997)
- [21] G. Barbarino et al., INFN Eloisatron Project, 36th Workshop, Erice, Italy, Nov 1-7, 1997.
- [22] R. Bellotti et al., Nucl. Instr. Meth. A 305(1991) 192
- [23] E. Barbarito et al., Nucl. Instr. Meth. A 365 (1995) 214
- [24] E. Barbarito et al., Nucl. Instr. Meth. A 357 (1995) 588
- [25] I. Lehraus et al., Nucl. Instr. Meth. 153 (1978) 347
- [26] D. Buskulic et al., Nucl. Instr. Meth. A 360 (1995) 481
- [27] T. Ludlam et al., IEEE Trans. Nucl. Sci. 28 (1981)
- [28] E. O'Brien et al., IEEE Trans. Nucl. Sci. 40 (1993) 153
- [29] A. Imanishi et al., Nucl. Instr. Meth. A 367 (1995) 244
- [30] Chorus Collaboration, CERN/PPE/93-131 (1993)
- [31] KLOE Collaboration, LNF 92/019
- [32] R. DeSalvo et al., Nucl. Instr. and Meth. A 315 (1992) 375
- [33] G. Martellotti, private communications
- [34] C. De Marzo et al., Nucl. Instr. Meth. 217 (1983) 405; H. Fessler et al., Nucl. Instr. Meth. 228 (1985) 303, Nucl. Instr. Meth. 240 (1985) 284;
- [35] M. Adams et al., Nucl. Instr. Meth. A 366 (1995) 263
- [36] M. Adams et al., Nucl. Instr. Meth. A 378(1996) 131
- [37] Winston, Progress in Optics 27 (1989) 161
- [38] G. Battistoni et al., INFN/AE-03/98 (1998)